Development of In Situ Formed Metal Pyrophosphates (MP$_2$O$_7$, Where M = Sn, Ti, and Zr)/PA/PBI Based Composite Membranes for Fuel Cells

Zehua Wang, Jin Zhang, Shanfu Lu, Yan Xiang, Zongping Shao, and San Ping Jiang**

Development of high temperature polymer electrolyte membrane fuel cells (HT-PEMFCs) at elevated temperatures is important for the enhancement of tolerance toward CO impurities and for the development of non-precious metal catalysts. The key challenge in such HT-PEMFCs is the high temperature polymer electrolyte membranes. Herein, the development of in situ formed metal pyrophosphates (MP$_2$O$_7$, where M = Sn, Ti, and Zr) in phosphoric acid doped polybenzimidazole (PA/PBI) composite membranes for HT-PEMFCs is reported. The formation mechanism of MP$_2$O$_7$, and characteristics of MP$_2$O$_7$/PA/PBI composite membranes are studied in detail. In contrast to the rapid decay in performance of pristine PA/PBI membrane cells, the in situ formed MP$_2$O$_7$/PA/PBI composite membranes show significantly higher proton conductivity, improved performance, and stability at elevated temperatures of 200–250 °C. The best results are obtained on the in situ formed SnP$_2$O$_7$/PA/PBI composite membrane cells, exhibiting a high peak power density of 476 mW cm^{-2} and proton conductivity of 51.3 mS cm^{-1} at 250 °C. The excellent durability of SnP$_2$O$_7$/PA/PBI composite membrane is due to the uniform distribution of in situ formed SnP$_2$O$_7$ nanoparticles in PBI membranes and the formation of a gel-like region, thin and irregular amorphous layer on the SnP$_2$O$_7$ with the high acid retention ability. This effectively alleviates the PA leaching at elevated temperatures of the new HT-PEMFCs.

Z. Wang, Z. Shao, S. P. Jiang
WA School of Mines: Minerals
Energy & Chemical Engineering
Curtin University
WA 6102, Australia
E-mail: s.jiang@curtin.edu.au

J. Zhang, S. Lu, Y. Xiang
Beijing Key Laboratory of Bio-inspired Energy Materials and Devices
School of Space and Environment
Beihang University
Beijing 100191, P. R. China
E-mail: lusf@buaa.edu.cn

S. P. Jiang
Foshan Xianhu Laboratory of the Advanced Energy Science
and Technology Guangdong Laboratory
Foshan 528216, P. R. China

1. Introduction

Proton exchange membrane fuel cells or more commonly known polymer electrolyte membrane fuel cells (PEMFCs) are one of the most efficient clean energy conversion devices and have been extensively used as power source for electric vehicles and portable electronic devices.[1] PEMFCs operating at temperatures higher than 100 °C or high temperature PEMFCs (HT-PEMFCs) possess adequate CO tolerance, high reaction kinetics and promising potential for the utilization of non-precious metal electrocatalysts.[2] Among them, phosphoric acid doped polybenzimidazole (PA/PBI) based HT-PEMFCs are the most successful, showing good performance with peak power density (PPD) of 500–800 mW cm^{-2} and long-term stability over 18 000 h under H$_2$/Air at the temperature range of 140–160 °C.[3] As a Brønsted base in comparison with PA, each PBI polymer repeat unit (PRU) can bound 2 PA molecules at its basic functional sites through acid–base complexation.[3a] Generally, PBI membrane soaked in concentrated PA solution can reach to a PA level (ADL) of about 6–11 PA/PRU, and the excess PA molecules are so-called the free PA.[3a,c,4] In PA/PBI membranes, protons are transferred through the rearrangement of hydrogen bonds between PA molecules and PBI skeleton, which mainly depends on the presence of doped PA molecules.[4,5] At low ADL, the transfer of protons mainly occurs between the basic N-H sites of PBI polymer and the PA anions.[6] In the case of high ADL, free PA in membrane can form the H$_3$PO$_4$/H$_2$PO$_4^-$ pathway, which is beneficial to the proton transfer and improve the conductivity.[3a] For instance, the conductivities of the PA/PBI based HT-PEMFCs are 50, 150, and 240 mS cm^{-1} at160 °C when the ADLs are of 6, 11, and 30 PA/PRU, respectively.[6,7] However, under anhydrous conditions, the self-dissociation of PA generates phosphoric oxoacid charge carrier of H$_2$PO$_4^-$.[8] At the same time, the dehydration of PA at high temperatures will also form hydrogen phosphate anions, such as H$_2$P$_2$O$_7^{2-}$ or H$_3$P$_3$O$_{10}^{2-}$.[3b,9] Unfortunately, the migration of these anions due to the electroosmotic drag during the fuel cell operation always leads to the rearrangement of PA in membrane.[8,9] Although those vehicular ions also contribute to the conductivity of fuel cell, the inevitable movement would

ADVANCED
SCIENCE NEWS

www.advancedsciencenews.com

ADVANCED
SUSTAINABLE
SYSTEMS

www.advsustainsys.com

result in the PA leaching and flooding in the anode side and the shortage in the cathode side, decreasing the proton conductivity and limiting the full contact of Pt with oxygen and further reducing the performance and stability of cells.[8]

Combination of PEMFCs and methanol steam reformer (MSR) utilizes methanol as hydrogen fuel source, which effectively overcomes technical and economic barriers of H_2 storage, transfer and distribution for fuel cell vehicle and portable applications.[10] Liquid based fuels such as methanol and ethanol have a much higher volume energy density of 15.6 and 20.9 MJ L^{-1} at ambient temperatures than H_2 gas of 5.6 MJ L^{-1} under 700 bar.[11] In comparison, the endothermic reforming of methanol occurs at 220–300 °C to reach sufficient kinetics, which lead to inability to combine with the conventional fuel cell stack without the regulation of thermal management devices.[12] Therefore, increasing the operation temperature of PEMFCs to 250–300 °C is necessary to achieve effective thermal integration with MSR.[10b,12] Increasing the cell operating temperatures can also substantially increase the kinetics of oxidation reactions of alcohols of direct alcohol fuel cells.[13] However, an increase in operation temperature of PA/PBI based HT-PEMFCs would accelerate the evaporation of PA and deteriorate the cell performance. Yu et al. observed ten times increase in the loss rate of PA at the cathode when the temperature enhanced from 160 to 190 °C.[14] Li et al. investigated the conditions affecting acid content during long-term operation, and found that high temperature, gas flow volume and current density contribute to the accelerated PA leaching.[3a,15] The PA loss via evaporation associated with the increased temperature and accumulated gas flow mainly results in the increasing of area-specific series resistance (ASR) in membrane.[3b,15] Meanwhile, high current density also has an influence of increased humidity, charge transfer, and water production in membranes, further exacerbating the deterioration of fuel cell performance.[15] Therefore, to obtain long-term stability, HT-PEMFCs need to be maintained at a lower current density of 200 mA cm^{-2} and appropriate temperature of 160 °C to minimize the negative effects of PA evaporation and dehydration.[3a,6,14,15]

Doping inorganic nanoparticles into PA/PBI membranes is a promising approach to alleviate PA loss at elevated temperature.[3a,16] By introducing hygroscopic fillers including clay, SiO_2, TiO_2, and ZrO_2, PA molecules would be bounded into the membrane through the introduced trapping sites and hydrogen bounds on the filler surfaces.[16a,17] For example, Lobato et al. fabricated a modified TiO_2/PBI composite membrane and showed a lower PA loss rate of 0.6 wt% calculating from the exhaust gas for over 1200 h.[18] Metal phosphate materials, such as metal pyrophosphates and phosphosilicate, have also been introduced into PBI polymer to form composite membranes.[19] Ooi et al. synthesized TiP_2O_7/PBI composite membrane and reported the acid retention ability improved from 12.8% in pristine PBI to 31.2% with addition of 1 wt% TiP_2O_7.[19a] Nevertheless, the proton conductivity of pure metal pyrophosphates (MP_2O_7, where M = Si, Zr, Ti, and Sn) is generally low in the range of ≈10^{-9}–10^{-8} S cm^{-1} at around 300 °C.[20] Among them, SnP_2O_7 attracted more attention because of the higher proton conductivity than other MP_2O_7.[21] Theoretical calculations by Kreller and Foran et al. revealed that the bulk crystalline phase of SnP_2O_7 do not contribute significantly to

the proton conductivity as these materials do not contain structural protons.[20b,22] Although doping low-valent cations, such as In^{3+}, was shown to assist crystalline material to incorporate protons from environment over 600 °C, the introduced cations do not enhance the mobility of proton as the discontinuous hydrogen bonds are difficult to form a network for transferring protons.[20b,23] Interestingly, the presence of residual phosphate or phosphoric acid has significant effect on the proton conductivity of metal pyrophosphates prepared by calcination. For example, the proton conductivity of $Sn_{0.9}In_{0.1}P_2O_7$ increased to 1.0×10^{-2} S cm^{-1} with a high phosphate to metal (P/M) ratio of 2.81.[23a] It has been shown that residual acid can form an amorphous layer on particle surface, which has a good and stable ionic conductivity at the temperature over 200 °C.[24] Nevertheless, the direct grinding of PBI and SnP_2O_7 prepared from the calcination method also causes the breakage of composite membrane due to the neutralization reaction between basic PBI and formed phosphors-rich layer.[25]

In recent years, we found that in situ formed phosphotungstic acid–meso-silica/PBI composite membrane shows an excellent performance and stability at operating conditions of 200 °C for 2700 h, and the in situ formed phosphosilicate nanoclusters in the composite membranes offer abundant hydroxyl groups, which alleviates the PA leaching, achieving a very low cell voltage degradation rate of as low as 27 µV h^{-1}.[26] Herein, we carried out the detailed study of the in situ formation of metal pyrophosphates (MP_2O_7 where M = Zr, Ti, and Sn), fabrication and characterization of the in situ formed MP_2O_7/PA/PBI composite membrane cells. In comparison with TiO_2 and ZrO_2, SnO_2 has the slowest reaction rate with PA, which facilitates a uniform distribution of in situ formed SnP_2O_7 nanoparticles within PBI membranes. The as-synthesized SnP_2O_7/PA/PBI based membrane cells achieved an excellent PPD of 475.6 mW cm^{-2} and high proton conductivity of 51.3 mS cm^{-1} at elevated temperature of 250 °C.

2. Result and Discussion

2.1. Characteristic of Pyrophosphate (MP_2O_7)

The formation process of MP_2O_7 between metal oxides (SnO_2, TiO_2, and ZrO_2) and PA at different temperatures was investigated by X-ray diffraction (XRD) measurement and the results are shown in **Figure 1**. The results show that $Ti(HPO_4)_2 \cdot H_2O$ and $Zr(HPO_4)_2 \cdot H_2O$ intermediates are initially formed at temperature of 160 °C for both TiO_2-PA and ZrO_2-PA samples after calcined for 4 h and the reaction is completed at 200–220 °C (Figure 1b,c), which quickly dehydrated to TiP_2O_7 and ZrP_2O_7 when the temperature increased to 240 and 220 °C, respectively. This is consistent with that reported in the literature.[27] In the case of TiO_2-PA samples (see Figure 1b,e), results deliver a two-step dehydration of $Ti(HPO_4)_2 \cdot H_2O$ (JCPDS: 33–1380). The initial dehydration occurred at 220 °C forms anhydrous $Ti(HPO_4)_2$ phase (JCPDS: 32–1369), which is related to the loss of one water molecule. Subsequently, a second condensation process occurred with the loss of water molecules until 250 °C, resulting in the formation of TiP_2O_7 phase (JCPDS: 38–1468).[27a] However, only one XRD peak related to
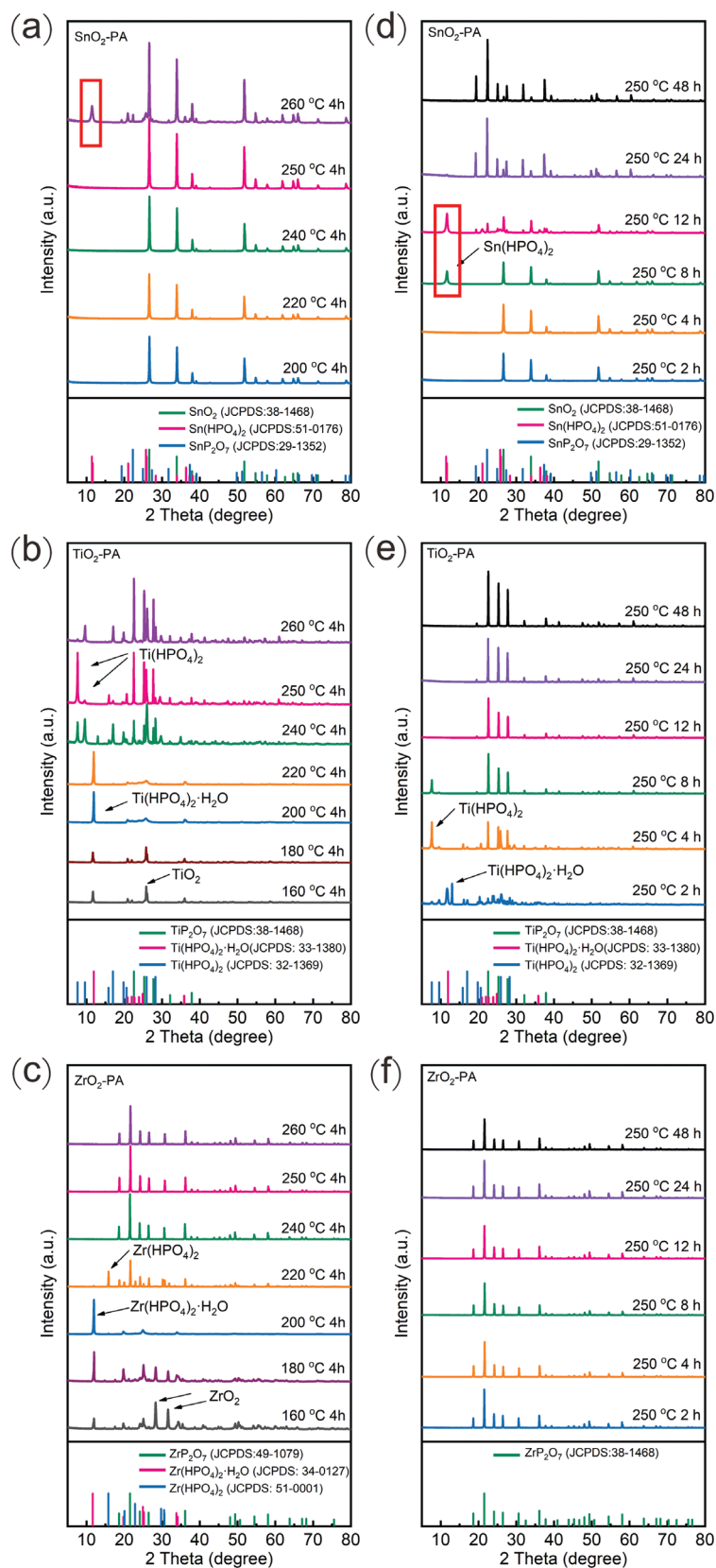
Figure 1. XRD patterns of a) SnO$_2$-PA, b) TiO$_2$-PA, and c) ZrO$_2$-PA synthesized at the temperature range of 160–260 °C for 4 h, and d) SnO$_2$-PA, e) TiO$_2$-PA, and f) ZrO$_2$-PA synthesized at 250 °C for 2 h to 48 h. The ratio of metal/phosphors was kept as 1/4.

**ADVANCED
SCIENCE NEWS**

www.advancedsciencenews.com

**ADVANCED
SUSTAINABLE
SYSTEMS**

www.advsustainsys.com

anhydrous $Zr(HPO_4)_2$ (JCPDS: 51–0001) can be found at 220 °C, see Figure 1c, indicating a fast dehydration in $Zr(HPO_4)_2 \cdot H_2O$ (JCPDS: 34–0217) crystalline phase. Note that pure ZrP_2O_7 phase was observed when the temperature increased to 240 °C (Figure 1c), which is lower than the formation temperature of pure TiP_2O_7 (250 °C for 12 h) and SnP_2O_7 (250 °C for 24 h). By contrast, the SnO_2 and PA mixture started to react at a higher temperature, forming the intermediate phase of $Sn(HPO_4)_2$ (JCPDS: 51–0176) after calcination at 260 °C for 4 h (Figure 1a). Nevertheless, the formation of $Sn(HPO_4)_2$ phase also depends on the duration of heat treatment. For example, $Sn(HPO_4)_2$ was formed after calcined at 250 °C for 8 h and further increase of heat treatment time will dehydrate $Sn(HPO_4)_2$, forming SnP_2O_7 (Figure 1d).[28] Therefore, the reaction of SnO_2, TiO_2, and ZrO_2 with PA start from the formation of $M(HPO_4)_2$ (M = Sn, Ti, and Zr) intermediates at lower temperature, which will gradually dehydrate to form MP_2O_7 with the increased temperature and duration. This can be shown in the following reaction steps:
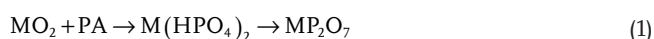
$$MO_2 + PA \rightarrow M(HPO_4)_2 \rightarrow MP_2O_7 \qquad (1)$$

Figure 2 shows the change of surface morphology and microstructure of MP_2O_7 formed at different temperatures. In the case of SnO_2-PA mixture, SnO_2 nanoparticles were uniformly distributed with the average diameter of 50 nm (see Figure 2a). The morphology and structure of SnO_2 nanoparticles were more or less the same after the heat-treatment with PA at 200 °C for 4 h, indicating no reaction between SnO_2 and PA, which is consistent with the XRD results of the mixture (Figure 1a). After calcination at 250 °C for 12 h, SnO_2 nanopar-

ticles disappear and instead nanosheets are formed (Figure 2c). The nanosheets are the typical feature of layered $Sn(HPO_4)_2$ intermediates.[29] Further increase of the heat treatment time to 48 h leads to the disappearance of nanosheets and the formation of irregular nanoparticles with the diameter in the range of 100–200 nm (Figure 2d). This is an indication of the dehydration of $Sn(HPO_4)_2$ phase and formation of SnP_2O_7, in good agreement with the XRD result.

In the case of the reaction between TiO_2 and PA, TiO_2 nanoparticles with diameter of ≈50 nm were aggregated to hexagonal shaped particles with the particle size of about 600 nm after calcined at 200 °C for 4 h, as shown in Figure 2f. This corresponds to the formation of $Ti(HPO_4)_2 \cdot H_2O$ intermediates.[27a] Moreover, it can be seen from Figure 2g that the hexagonal $Ti(HPO_4)_2 \cdot H_2O$ is not stable and decomposed gradually as the temperature rises from 200 to 250 °C, showing the molten phase on the surface. In titanium phosphates, the water content varies with the synthesis temperature; therefore, the dehydration of $Ti(HPO_4)_2 \cdot H_2O$ at 250 °C result in the variation of its crystalline structure, which is consistent with the XRD results.[30] $Ti(HPO_4)_2 \cdot H_2O$ is completely transformed into the TiP_2O_7 after heat treatment at 250 °C for 48 h, and at the same time, hexagonal nanoparticles continue to decompose into broken and irregular nanosheets, in an agreement with that reported.[27a,30] Hence, TiP_2O_7 nanosheets prepared by calcination of the TiO_2 and PA mixture undergo three stages at the temperature range of 200–250 °C according to scanning electron microscopy (SEM) and XRD analyses. First, regular and uniform hexagonal $Ti(HPO_4)_2 \cdot H_2O$ is emerged below 220 °C accompanied by the dramatic increase in the volume
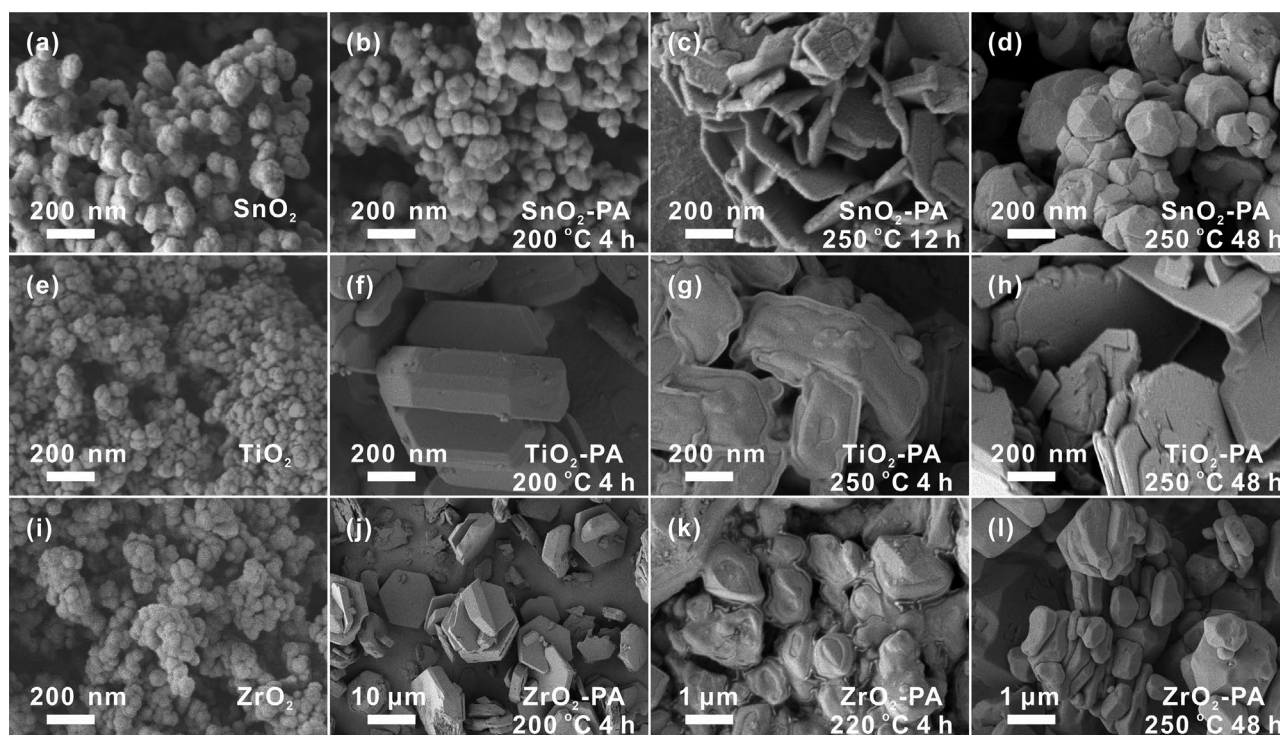

Figure 2. SEM images of a) SnO_2, e) TiO_2, and i) ZrO_2 nanoparticles before the heat treatment, b–d) SnO_2-PA, f–h) TiO_2-PA, and j–l) ZrO_2-PA mixture calcined at different temperatures for different periods.

of particles. Then, the gradual loss of water in homogeneous $Ti(HPO_4)_2 \cdot H_2O$ with the increase of temperature to 240 °C lead to the molten phase formation on the surface of collapsed particles. Finally the continuous heating up to 250 °C leads to the formation of TiP_2O_7 nanosheets via the gradual dehydration and decomposition of $Ti(HPO_4)_2$.

The morphology and structure variation of $Zr(HPO_4)_2 \cdot H_2O$ from ZrO_2 and PA reactions is similar to that of $Ti(HPO_4)_2 \cdot H_2O$, as shown in Figure 2i,j. However, ZrO_2 trends to transform into large particles (around 10 µm, see Figure 2j), which may limit the proton transfer as the lattice conduction is negligible. The dehydration of $Zr(HPO_4)_2 \cdot H_2O$ starts at 200 °C according to the XRD results in Figure 1c, consistent with that reported by Costantino et al.[31] This is also confirmed by the irregular and broken particles (see Figure 2j). The molten phase on the surface of ZrO_2-PA sample calcined at 220 °C for 4 h can be clearly seen, as shown in Figure 2k, which is ascribed to the formation of anhydrous $Zr(HPO_4)_2$ phase and the loss of absorbed water molecules between two crystalline layers.[31] Increasing the calcination temperature and time will also lead to the collapse of $Zr(HPO_4)_2$, thus, generating irregular particles of ZrP_2O_7 with the size from hundreds of nanometers to a few micrometers, as shown in Figure 2l.

As calcined SnO_2-PA, TiO_2-PA, and ZrO_2-PA mixtures post-treated with the same washing procedure were examined by high-resolution transmission electron microscopy (HR-TEM) and the results are shown in **Figure 3**. There are significant differences in the surface morphology of the synthesized SnP_2O_7, TiP_2O_7, and ZrP_2O_7 samples. In the case of SnO_2-PA (see Figure 3a–d), there is a thin and non-uniform amorphous layer attached on the surface of SnP_2O_7 nanoparticles, consistent with the result reported by Xu et al.[32] It has been found that this amorphous layer is unstable under the high accelerated voltage, which gradually disappeared on the SnP_2O_7 crystalline surface, as seen in the Figure 3c,d. The EDS mapping images (Figure 3i–l) also exhibit significant presence of oxygen and phosphorus elements on the surface, indicating that this amorphous layer should be phosphorus-rich species derived from PA.[32] Different to the amorphous layer formed on SnP_2O_7 particles, the surface layer on TiP_2O_7 particles is very uniform with the average thickness of 10 nm. The HAADF mapping images indicate the homogeneous distribution of titanium, oxygen and phosphorus elements in the surface and crystalline areas (Figure S1, Supporting Information), indicating that this layer appears to be semi-crystallized phase. In contrast to the surface morphology of both SnP_2O_7 and TiP_2O_7, ZrP_2O_7 particles show a clean surface with no additional amorphous layer (Figure 3h). The formation of core–shell structure with an irregular and thin amorphous layer surrounding SnP_2O_7 crystalline core is a distinctive characteristic of SnP_2O_7 phase formed between SnO_2 and PA.

As-synthesized SnP_2O_7, TiP_2O_7, and ZrP_2O_7 samples were studied by FTIR (see Figure S2a, Supporting Information). The broad peaks between 2000 and 3000 cm^{-1} and two small peaks at around 1600 cm^{-1} are the vibration of −OH groups, which may originate from the absorbed water
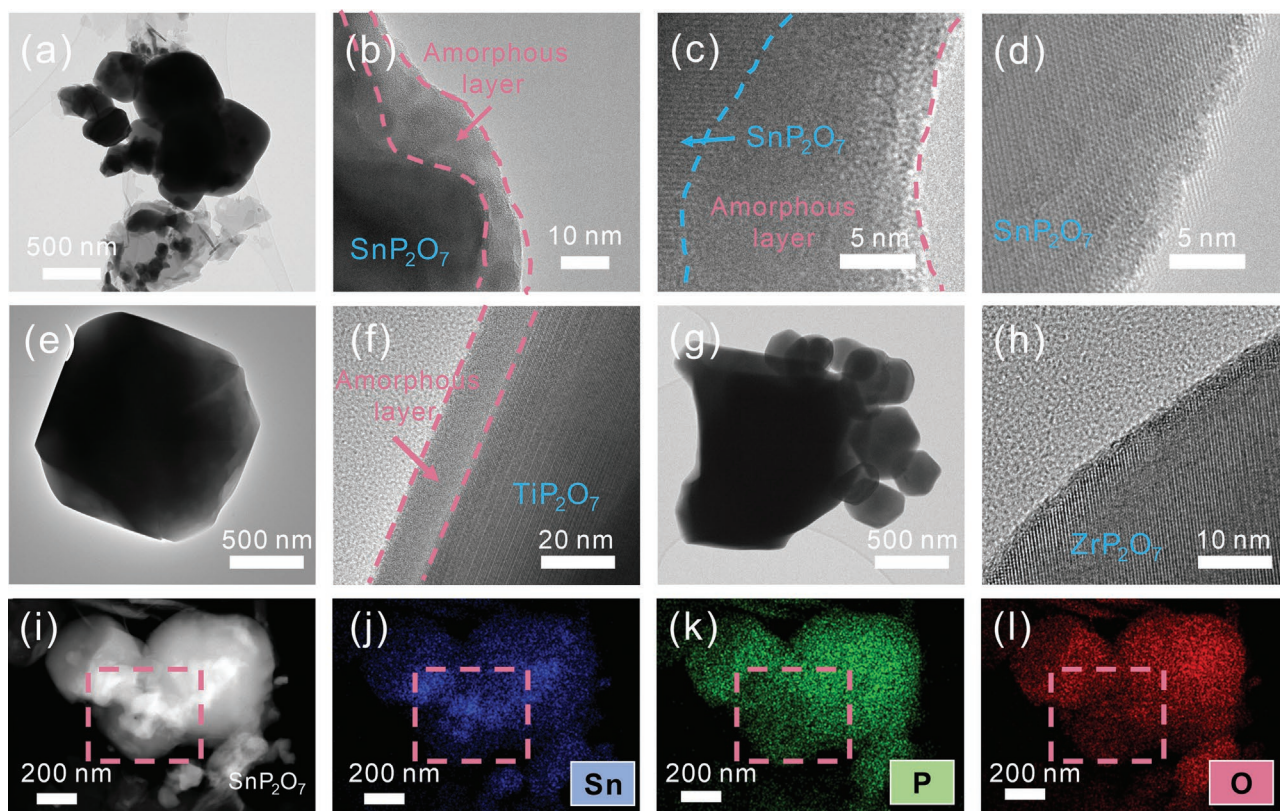

Figure 3. TEM and HR-TEM images of a–d) SnP_2O_7, e,f) TiP_2O_7, and g,h) ZrP_2O_7. i) A typical TEM image of SnP_2O_7 and the corresponding elemental mapping of j) tin (blue), k) phosphorus (green), and l) oxygen (red) elements.
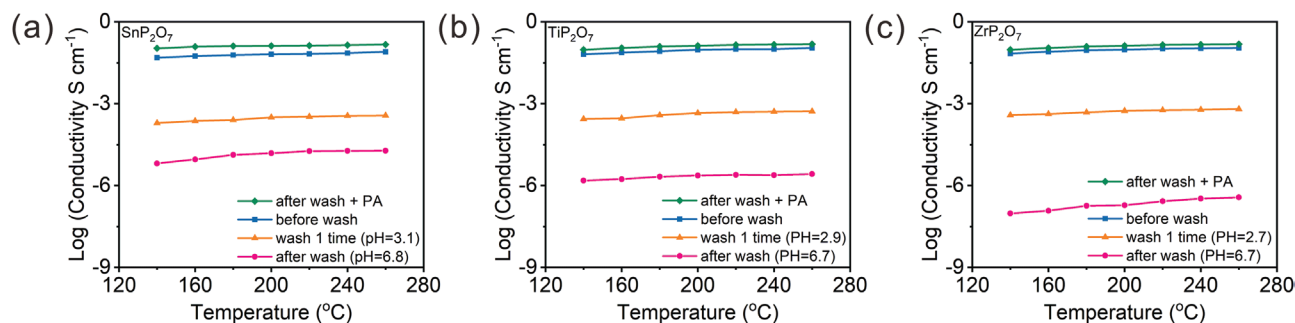
**ADVANCED
SCIENCE NEWS**
www.advancedsciencenews.com

**ADVANCED
SUSTAINABLE
SYSTEMS**
www.advsustainsys.com

Figure 4. Proton conductivity of a) SnP_2O_7, b) TiP_2O_7, and c) ZrP_2O_7 before and after washing treatment. The curves with diamond symbols indicate the pure MP_2O_7 phase after complete washing with PH value of 6.7–6.8 and PA mixture with the molar ratio of 1/2.

molecules, suggesting that the synthesized MP_2O_7 samples have a good hygroscopicity.[20,33] In the case of washed SnP_2O_7, two small peaks at around 1200 cm^{-1} were observed, which can be assigned to the deformation mode of P-OH group, indicating the presence of acid.[20a,32,33] The specific surface area of the as-prepared SnP_2O_7, TiP_2O_7 and ZrP_2O_7 was analyzed by Brunauer–Emmett–Teller (BET) method (Figure S2b, Supporting Information) and the corresponding N_2 adsorption and desorption isotherms were characterized by typical type-IV curves with slight H3 type hysteresis loop, indicating the existence of mesoporous structure.[34] Mesoporous structure in pyrophosphates would be beneficial to retain water and PA molecules through capillary condensation and therefore improve the proton conductivity.[34,35] Based on the BET analysis, the calculated specific surface areas of SnP_2O_7, TiP_2O_7, and ZrP_2O_7 were 10.82, 1.03, and 0.59 m^2 g^{-1}, respectively. SnP_2O_7 shows a much higher specific surface area than that of TiP_2O_7 and ZrP_2O_7 samples, consistent with the fine microstructure of SnP_2O_7 nanoparticles (see Figure 2).

The kinetics of the MP_2O_7 formation was studied by NH_3-TPD method and the results are shown in Figure S2c, Supporting Information. Obviously, SnO_2 contains two major peaks at 363.1 and 452.5 °C, indicating a desorption of NH_3 from strong acid sites on the surface.[36] By contrast, ZrO_2 exhibits a broad peak at around 100 °C with a downward platform at the temperature range of 200–700 °C, confirming that ZrO_2 is more basic.[37] The NH_3-TPD curve of TiO_2 sample is similar to that of ZrO_2, and a broad peak located at about 375.3 °C indicates the existence of acid sites. Therefore, the relative acidity trend is $ZrO_2 < TiO_2 < SnO_2$, which is consistent with the reported literatures.[38] According to the dissolution-nucleation mechanism based on the acid–base reaction,[39] metal ions are initially released from oxides into PA solution, thereby reacting with phosphate anions and forming metal hydrophosphates, in which the reaction is controlled by the dissolution step. MP_2O_7 phase is formed from the subsequent dehydration of hydrophosphates at elevated temperatures. Therefore, it can be concluded that the formation of SnP_2O_7 takes a longer process with higher energy barrier than that of TiP_2O_7, and ZrP_2O_7, thus requiring a higher heat-treatment temperature to accelerate the reaction. The high energy barrier could also be the reason for the formation of irregular and thin amorphous layer on the surface of SnP_2O_7 nanoparticles (see Figure 3a–d). This is consistent with the XRD and SEM studies as shown above.

2.2. Proton Conductivity

The proton conductivity of MP_2O_7 samples before and after washing was measured at the temperature range of 140 – 260°C and the results are shown in **Figure 4**. In the figure, the proton conductivity values of MP_2O_7 samples after complete washing with molar ratio of 1/2 and as-prepared MP_2O_7 after 1 washing and complete washing with indicative pH were also added. For MP_2O_7 calcined at 250 °C for 24 h, no obvious change in the characteristic XRD peaks was detected, indicating washing has no effect on the crystalline phase of the synthesized MP_2O_7 (Figure S3, Supporting Information). The proton conductivity of as-synthesized SnP_2O_7, TiP_2O_7, and ZrP_2O_7 obtained at 250 °C before washing reached to 1.0×10^{-1} S cm^{-1} at 140 °C and increased slightly with the measurement temperature. However, the conductivity of MP_2O_7 samples after washing treatment dramatically dropped. For example, the as-synthesized SnP_2O_7 sample after complete washing shows a proton conductivity of 1.91×10^{-5} S cm^{-1} at 260 °C, which is five orders of magnitudes lower than the conductivity of as-synthesized sample before washing, in good agreement with the proton conductivity of $\approx 10^{-6}$ S cm^{-1} of pure SnP_2O_7 powder reported by Li et al.[20a] The proton conductivity of MP_2O_7 samples is also dependent on the washing procedure. After washing one time, the proton conductivity of as-prepared SnP_2O_7 is 4.0×10^{-4} at 260 °C, significantly higher than that of pure SnP_2O_7 phase. The high conductivity is clearly due to the presence of PA in the sample, as indicated by the low pH value of 3.1 as compared to the pH value of 6.8 for the completely washed sample (Figure 4a). The results show that the presence of PA is responsible for the high proton conductivity of as-prepared SnP_2O_7 sample. Figure 4b shows the proton conductivity of synthesized TiP_2O_7 before and after washing procedure measured at 260 °C, decreased significantly from initial 0.1 S cm^{-1} before washing to 2.7×10^{-6} S cm^{-1} after washing. The values of conductivity in the washed TiP_2O_7 powder can be recovered with the addition of PA, reaching to ≈ 0.1 S cm^{-1} in the temperature range of 140–260 °C. Similarly, ZrP_2O_7 also exhibited the importance of the presence of phosphate phase in the proton conductivity of samples varied between 0.1 and 3.7×10^{-7} S cm^{-1} as a function of washing procedures (see Figure 4c).

The proton hopping through the bulk crystalline lattice defects has been confirmed to contribute little to the excellent conductivity of the as-synthesized MP_2O_7.[20b] This is supported by the very low conductivity of 2.7×10^{-6} and 3.7×10^{-7} S cm^{-1}

at 260 °C measured on completely washed TiP_2O_7 and ZrP_2O_7 samples, respectively. However, SnP_2O_7 sample shows a higher proton conductivity of 1.9×10^{-5} S cm^{-1} under identical test conditions. As shown in Figure 3b, a distinctive presence of a thin and irregular amorphous layer on the SnP_2O_7 particles may indicate the retention of a small amount of acid in the surface, forming an proton-conducting layer around the surface of SnP_2O_7 nanoparticles.[32] The formation of such core–shell structure would be beneficial for the proton conductivity and this explains the high proton conductivity of SnP_2O_7 phase as compared to TiP_2O_7 and ZrP_2O_7.

2.3. Characteristics of Composite Membranes

Before the characterization of the composite membranes, the in situ formation processes of MP_2O_7 phase in the composite membranes were investigated by XRD patterns of the as-prepared composite membranes after heat treatment at 250 °C from 12 to 48 h and the results are shown in **Figure 5**. Pristine SP-1/4, TP-1/4, and ZP-1/4 composite membranes showed a broad peak in the range of 15–30°, which is related to the amorphous structure of PBI, while sharp peaks are associated with the oxide fillers. Small peaks at 2θ of 19.3°, 22.3°, 24.9° observed for SP-1/4 membrane heat-treated at 250 °C for 36 and 48 h are associated with SnP_2O_7 (JCPDS: 29–1352), indicating the in situ formation of SnP_2O_7 phase in PBI matrix (Figure 5a). It is noticed that the XRD peak intensity of SnO_2 in SP-1/4 composite membrane maintains sharp and strong feature even after reaction for 36 h, and several small peaks were also observed in samples sintered for 48 h. This suggests that the reaction rate of SnO_2 with PA in the membrane is relatively slow. Different from SP-1/4 membrane, TP-1/4 and ZP-1/4 composite membranes show only diffraction peaks associated

with TiP_2O_7 and ZrP_2O_7 crystalline phase after heat-treatment for 36 h (see Figure 5b,c) and no peaks associated with TiO_2 and ZrO_2 phases were observed. This indicates that the in situ formation of MP_2O_7 phase in the composite membrane during the heat treatment of the composite membrane at 250 °C is also dependent on the nature of the oxides. In the case of ZP-1/4, the particle size of ZrP_2O_7 was estimated to be 5 μm using the Scherrer formula from XRD measurement (Figure 5c), which is much higher than ≈300 nm and 3 μm calculated for the in situ generated SnP_2O_7 and TiP_2O_7 particles, respectively. Nevertheless, the in situ formed MP_2O_7 phases in PBI polymer matrix show similar characteristic peaks in comparison with the XRD results of as-prepared MP_2O_7 powders (see Figure 1) under the same synthesis condition, and the only differences are in the lower peak intensity and broader peak width of the in situ formed MP_2O_7 phases in PBI polymer matrix. This indicates that PBI matrix does not inhibit the metal pyrophosphate phase formation but alleviate the aggregation of in situ formed MP_2O_7 phase.

To identify the in situ formation mechanism of TiP_2O_7 and ZrP_2O_7 in PBI matrix, PA doped TiO_2/PBI and ZrO_2/PBI composite membrane were calcined at the temperature range of 180–220 °C for 2 h, and the corresponding XRD patterns are shown in Figures S4 and S5, Supporting Information. Obviously, peak intensity associated with TiO_2 and ZrO_2 nanoparticles increases with the increase of filler content. The results show that $Ti(HPO_4)_2$ (JCPDS: 32–1370) was initially transformed from TiO_2 nanoparticles at 180 °C and partially decomposed to TiP_2O_7 when the temperature increased to 250 °C, which is similar to the formation of TiP_2O_7 in the heat-treated $TiO_2/$ PA mixture. In comparison with the XRD data of $Zr(HPO_4)_2$ and ZrP_2O_7 phases observed in the sintered ZrO_2/PA sample, the XRD peaks related to $Zr(HPO_4)_2$ crystalline phase in calcined ZrO_2/PBI composite membrane were higher and clearly
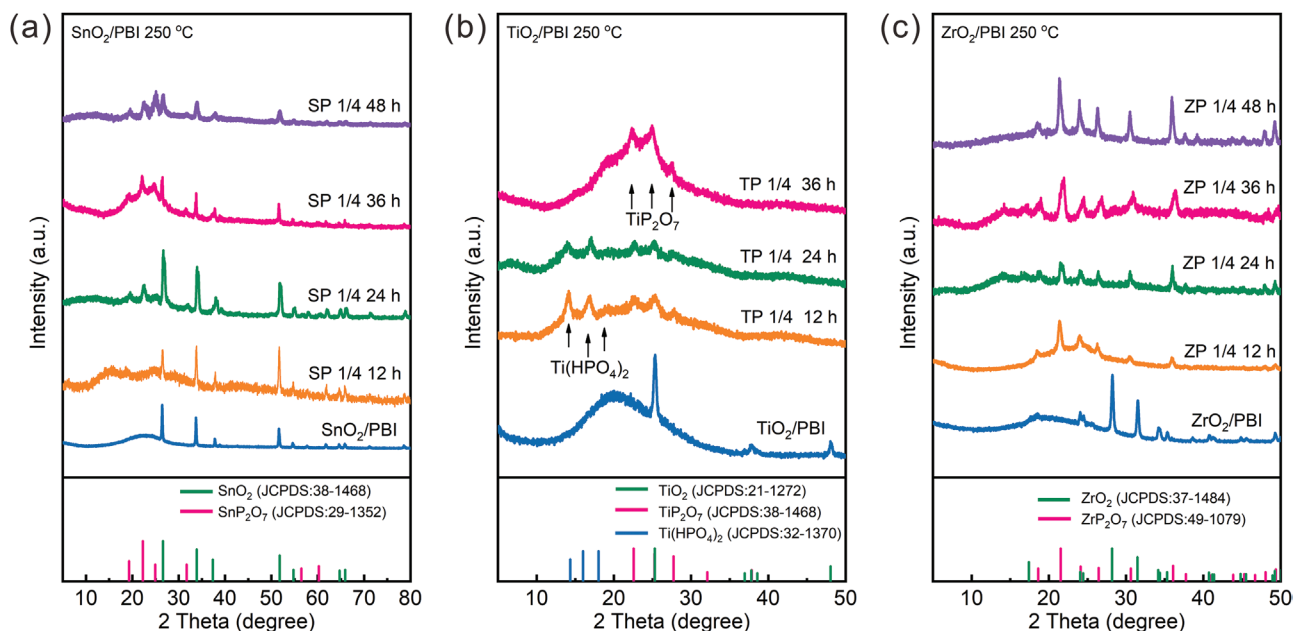

Figure 5. XRD patterns of PA doped a) SP-1/4, b) TP-1/4, and c) ZP-1/4 composite membranes heat-treated at 250 for 12–48 h. Composite membranes were washed by DI water and ethanol to remove excess PA in the membranes.
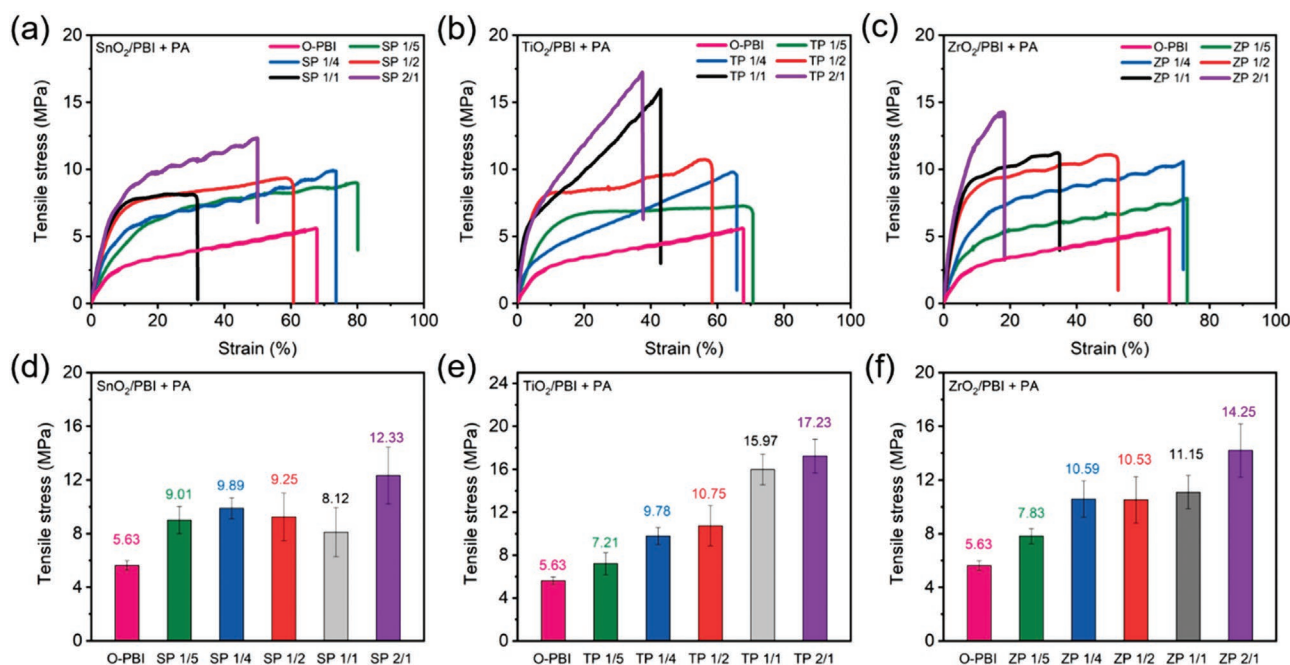
**ADVANCED
SCIENCE NEWS**

www.advancedsciencenews.com

**ADVANCED
SUSTAINABLE
SYSTEMS**

www.advsustainsys.com

Figure 6. Stress–strain curves and corresponding comparison charts of pristine O-PBI and composite membranes of a,d) SP, b,e) TP, and c,f) ZP with various oxide/PBI molar ratios after immersing PA at 80 °C for 3 days.

separated, but disappeared after further heat treatment at 250 °C for 12 h. Therefore, the prior polarization treatment for SnO_2/PBI, TiO_2/PBI, and ZrO_2/PBI was selected at 250 °C for at least 48 h to guarantee the in situ formation of MP_2O_7 phase in the composite membrane.

The PA doping treatment was carried out by immersing the pristine PBI and composite membranes in 85% PA solution at 80 °C for 3 days. Figure S6, Supporting Information, shows the volume swelling ratio, PA uptake, and PA doping level per unit volume of prepared membranes. In the case of pristine PBI membrane, the volume swelling ratio and PA uptake was about 140.4% and 214.3 wt%, respectively, corresponding to about 9.4 PA per PRU.[5] The relationship between metal oxide content and volume swelling ratio and PA uptake are shown in Figure S6a–c, Supporting Information, showing a decline trend of volume swelling ratio and PA uptake with the increase of oxide filler loading, varied in the range of 133.8–100.2% for volume swelling ratio of SP-1/5 to SP-2/1. The reduced volume swelling will result in the improved mechanical strength of membrane, which is a critical aspect of operational stability of fuel cell.[40] The PA uptake of SP-2/1 was 129.3 wt%, corresponding to 5.7 PA per PRU. The PA doping level per unit volume of pristine PBI and oxide filler content is shown in Figure S6d–f, Supporting Information. For example, it showed an increase PA doping level varied from 1.29 to 1.31 g cm^{-3} for pristine PBI to SP-1/4, while it declines with the increase in the loading of SnO_2 filler, reveling 1.09 g cm^{-3} doping level in SP-2/1. In addition, the PA doping level of TP-1/4 and ZP-1/4 is 1.34 and 1.35 g cm^{-3}, respectively, indicating a positive influence of the oxide filler on the PA doping of composite membrane due to the presence of the hygroscopic group on the oxide surface.[3a,41]

The mechanical robustness of the membranes is an important factor in the practical application of PEMFC as the mechanically weak membrane may crack during the operation, resulting in gas leakage and therefore degrading the performance and stability of fuel cell stack.[3b] Mechanical properties of pristine and composite membranes after doping PA at 80 °C for 3 days are shown in **Figure 6**. The pristine PBI exhibited the lowest tensile stress of 5.63 MPa than that of composite membranes due to the highest swelling. The reduced tensile strength and increased elongation of PBI membrane are most likely caused by the plasticizing effect of the doped PA molecules.[42] On the other hand, the tensile stress of SnO_2/PBI composite membranes increased to 12.33 MPa in the case of SP-2/1 composite membrane, while the elongation dramatically decreased to 32% (Figure 6a,d). This may be related to the filler-filler crosslinks from oxides and lower PA doping level of the composite membrane.[40,42] The tensile stress and elongation of TiO_2/PBI composite membranes after PA doping varied between 7.21 and 17.23 MPa and 71.2% to 37.6%, respectively. Similar mechanical properties are also observed in ZrO_2/PBI composite membranes, showing an 8.62 MPa increase of tensile stress and 41.5% decrease of elongation in ZP-2/1 as compared to pristine PBI.

To evaluate the influence of PA retention capability in the in situ formed $MP_2O_7/PA/PBI$ composite membranes, an acid leaching test was carried out by recording the weight loss of membranes placed in a constant temperature and humidity chamber at 80 °C and 70% RH.[43] All composite membranes were fabricated with clean MP_2O_7 to minimize the influence of residual acid within in situ formed MP_2O_7 in membranes. As seen from **Figure 7**, the PA retention of pristine PBI membrane is 61.2%. In comparison, the adding of MP_2O_7 fillers enhance the PA retention capability of PA/PBI membrane, showing 73.2% for SnP_2O_7, 70.2% for TiP_2O_7, and 69.1% for ZrP_2O_7, respectively. Among them, SnP_2O_7 fillers show the best acid
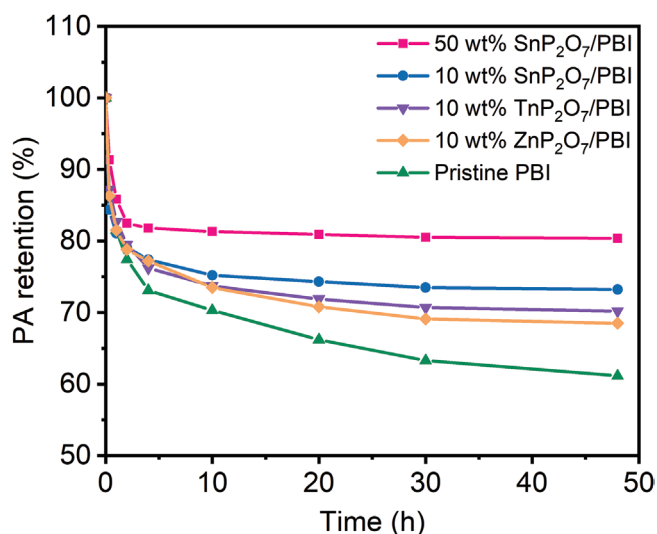
Figure 7. The PA retention capacity curves of pristine PA/PBI membrane and 10 and 50 wt% SnP$_2$O$_7$/PA/PBI, 10 wt% TiP$_2$O$_7$/PA/PBI, and 10 wt% ZrP$_2$O$_7$/PA/PBI composite membranes. All membranes were placed in a constant temperature and humidity chamber at 80 °C and 70% RH.

retention capability. In addition, composite membrane with 50 wt% loading of SnP$_2$O$_7$ has the highest PA retention of 80.4%, indicating that the in situ formed MP$_2$O$_7$ can effectively alleviate the leaching of PA from the membrane.

Figure 8 shows the SEM images of cross-section of pristine SP-1/4, TP-1/4, and ZP-1/4 composite membranes and heat-treated samples at 250 °C for 48 h, respectively. The corresponding surface microstructures are given in **Figure 9**. Pristine composite membranes were characterized by dense and smooth surface (Figure 9a,d,g). By contrast, the surface of composite membrane became rough, accompanied by distinct particles with the increase of oxide content (Figures S7–S9, Supporting Information). The backscattering electron images shown in Figure 8 confirm the homogeneous distribution of metal oxide fillers in PBI matrix, where particles in white color represent inorganic phases while dark phase corresponds to the PBI matrix. In the case of heat-treated SP-1/4 membrane (Figure 8d), SnO$_2$ nanoparticles were transformed to SnP$_2$O$_7$ in PBI membrane with no obvious aggregation. On the other hand, after the calcination at 250 °C for 12 h, agglomeration of particles occurs on the membrane surface of TP-1/4 and ZP-1/4 and the particle size of TiP$_2$O$_7$ and ZrP$_2$O$_7$ is as large as 2 µm (Figure 9e,h). This may be the reason for the formation of cracks and isolated pores in membranes (Figure 8e,f). Moreover, further increase in the heat treatment time to 48 h led to the significant agglomeration of in situ generated ZrP$_2$O$_7$, forming a loose shell of oxide material covered on the surface of PBI membrane (Figures 8f and 7i). Formation of such distinct oxide layer would result in the deterioration of performance in the composite membranes as the proton conductivity of ZrP$_2$O$_7$ crystalline phase is negligible. In addition, formed pores or cracks in membrane can promote the PA leaching, which also leads to the deterioration of mechanical robustness in composite membranes.[42]

2.4. Electrochemical Performance of Composite Membrane Cells

The proton conductivity of pristine PA/PBI and composite MP$_2$O$_7$/PA/PBI membranes after heat treatment at 250 °C for 48 h was measured and the results are shown in **Figure 10**. In the case of heat-treated PA/PBI membrane, the proton conductivity decreased from 47 mS cm^{-1} at 280 °C to 3.1 mS cm^{-1} when
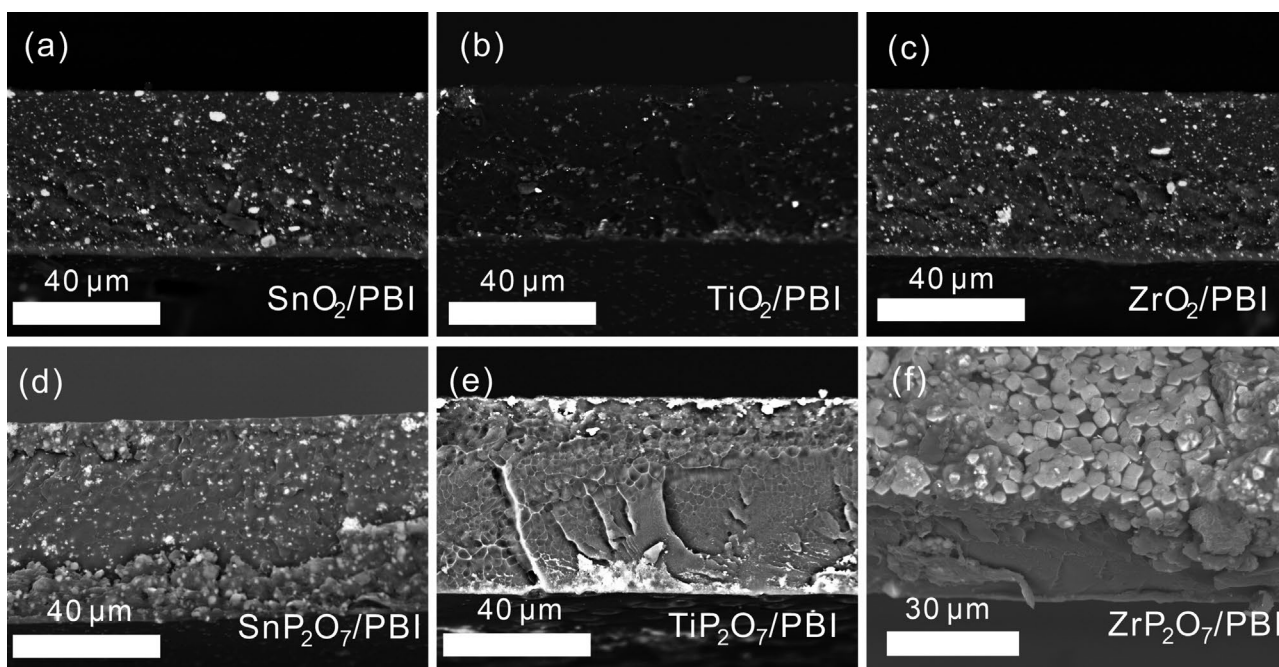

Figure 8. SEM images of cross-section of pristine a) SP-1/4, b) TP-1/4, and c) ZP-1/4 composite membranes and d–f) corresponding composite membranes after polarization at 250 °C for 48 h, respectively.
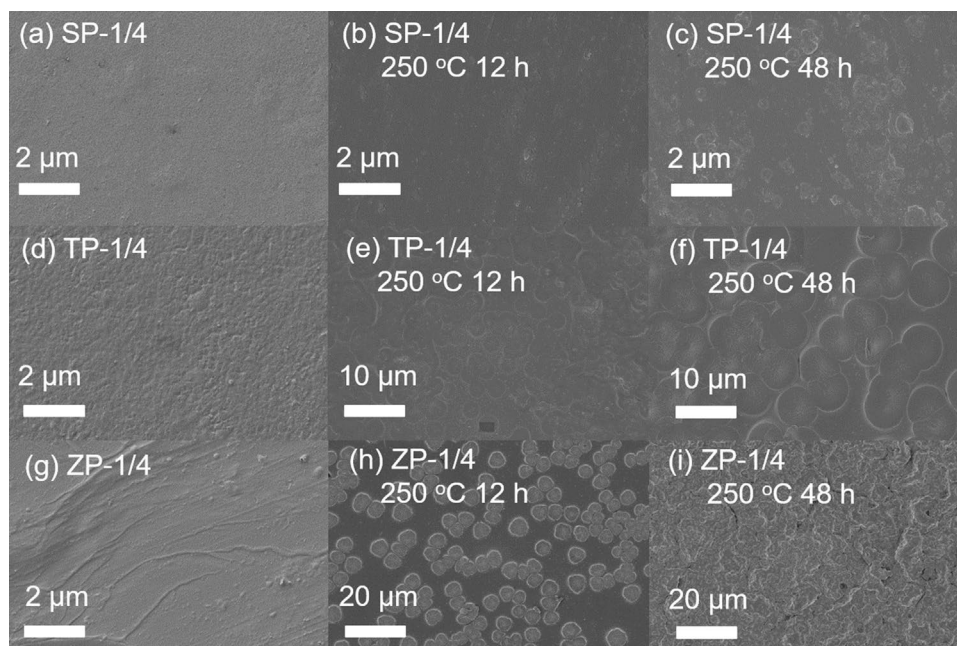
Figure 9. SEM images of the surface of a–c) pristine SP-1/4, d–f) pristine TP-1/4, and g–i) pristine ZP-1/4 and composites membrane after polarization at 250 °C for 12 and 48 h, respectively.
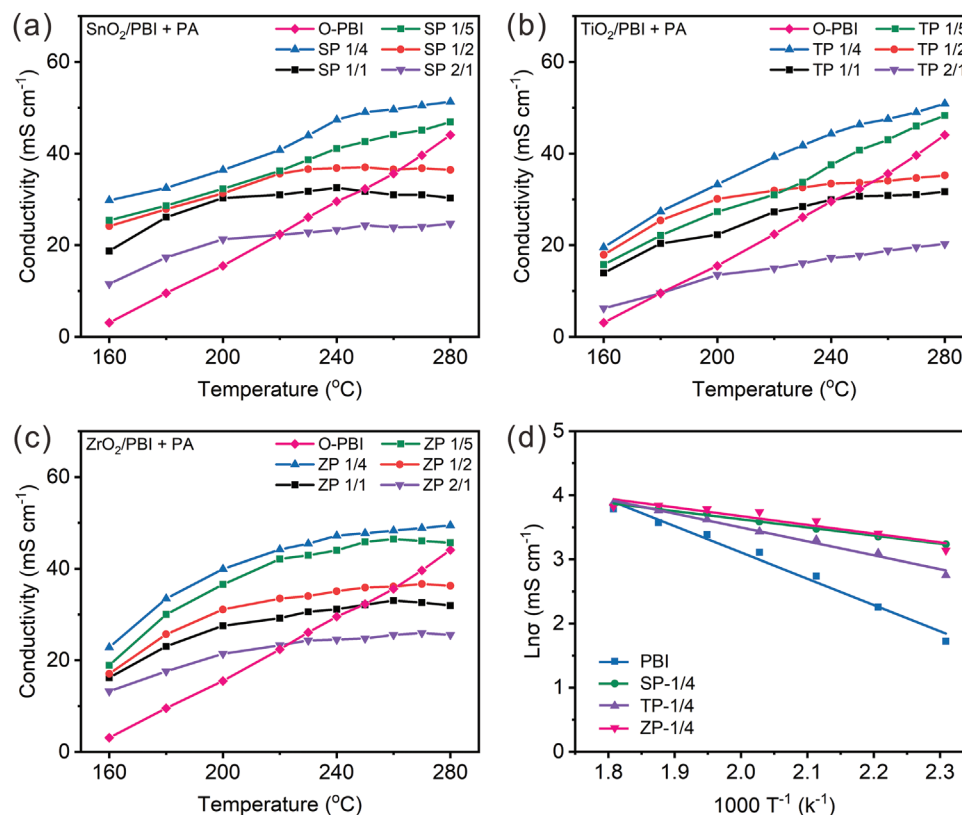

Figure 10. Proton conductivity of a) SnO_2/PBI composite membranes, b) TiO_2/PBI composite membranes, c) ZrO_2/PBI composite membranes. d) Arrhenius plots of pre-calcined PBI membrane, SP-1/4, TP-1/4, and ZP-1/4 composite membranes All composite membranes were pre-calcined at 250 °C for 48 h.

temperature dropped to 160 °C (Figure 10a), corresponding to a 93% reduction in conductivity. The conductivity of 3.1 mS cm^{-1} measured at 160 °C is also much lower than ≈50 mS cm^{-1} reported on stable PA/PBI membrane measured at 160 °C.[5] The proton conductivity of pristine PA/PBI membranes increased rather rapidly with temperature, but it is well known that the proton conductivity of pristine PA/PBI membranes deteriorates quickly during the operation of PEMFC above 200 °C due to the evaporation of PA at elevated temperatures.[3b,44] Very different to the behavior of pristine PA/PBI membrane, the proton conductivity of MP$_2$O$_7$/PBI/PA composite membranes shows a much lower dependence on the temperature in the temperature range studied. For instance, the SP-1/4 composite membrane showed a conductivity of 51.3 mS cm^{-1} at 280 °C and decreased to 29.7 mS cm^{-1} when the temperature reduced to 160 °C (Figure 10a), a 42% reduction in proton conductivity. This is substantially lower than 93% reduction in the case of pristine PA/PBI membranes. Similar behavior was also observed for the TP and ZP based composite membranes. However, the aggeration of TiP$_2$O$_7$ and ZrP$_2$O$_7$ particles forms loose shells on composite membrane surface, which decreases their proton conductivities. For example, in the case of TP-1/4 and ZP-1/4 composite membranes, the proton conductivity is 49.9 and 48.3 mS cm^{-1} at 280 °C, respectively, lower than that measured on SP-1/4 composite membranes. Nevertheless, the proton conductivity of the composite membranes is a strong function of the metal oxide to PBI ratios. The in situ formation of MP$_2$O$_7$ in the PA/PBI membrane consumed the absorbed PA, resulting in inferior proton conductivity below that of pristine PBI membrane when the molar ratio of oxide/PBI enhances to 1/2. For example, the proton conductivity of SP-1/2, SP-1/1, and SP-2/1 is 36.4, 30.3, and 24.7 mS cm^{-1} at 280 °C, lower than 47 mS cm^{-1} at 280 °C measured on pristine PA/PBI membranes (see Figure 10a). However, increasing the PBI content (i.e., low metal/PBI ratios) increases the proton conductivity of the composite membranes.

Activation energy of proton conductivity of pristine and composite membranes was obtained using the Arrhenius plots of pre-calcined PA/PBI membrane, SP-1/4, TP-1/4, and ZP-1/4 composite membranes (Figure 10d). The activation energy (E_a) of the pristine PA/PBI membrane was calculated to 25.6 KJ mol^{-1}, indicating that the Grotthuss mechanism become the dominant for proton conduction in membrane.[45] By comparison, the calculated E_a of composite membranes was 11.28 KJ mol^{-1} for SP-1/4, 16.17 KJ mol^{-1} for TP-1/4, and 13.18 KJ mol^{-1} for ZP-1/4, respectively, lower than that of pristine PA/PBI membranes. The reduced energy barrier for proton transfer in composite membranes may indicate the synergetic effect of in situ formed MP$_2$O$_7$ phase or nanoclusters in the composite membrane.[40,45,46]

The preliminary performance and stability were investigated on pristine and composite MP$_2$O$_7$/PA/PBI membrane fuel cells at 160 and 250 °C under a constant current load of 200 mA cm^{-2}, and the results are shown in **Figure 11**. In this case, the best performed composite membranes with metal/PBI ratio of 1/4 were used. The open circuit voltage (OCV) of pristine PA/PBI membrane cell is 0.923 V and the initial cell voltage is 0.613 V and stable at 160 °C under a current load of 200 mA cm^{-2} (Figure 11a), which is similar to the results reported by Li

et al.[19b] With the temperature raised to 250 °C, the cell voltage dropped to 0.412 V under the same current load and decreased quickly to 0.2 V after polarized for 33 h with a degradation rate of 6.42 mV h^{-1}. The initial PPD of PA/PBI membrane cell is 124.9 mW cm^{-2}, and decreased significantly to 65.2 mW cm^{-2} after tested at 250 °C for 33 h (Figure 11b). To further investigate the change in the properties of pristine PA/PBI membrane cells, electrochemical impedance spectroscopy (EIS) was conducted at a constant voltage of 0.6 V. The impedance of the cells is characterized by typical depressed semicircles, in which the high frequency intercept presents the total ohmic resistance of the cell (R_{ohm}) and the difference between the low and high frequency intercepts on the real axis indicates the total cell polarization resistance (R_P).[42] The results show that in the case of pristine PA/PBI membrane cells, the R_{ohm} increased significantly from 0.17 Ω cm^2 at 160 °C to 0.71 Ω cm^2 at 250 °C, which further increased to 1.65 Ω cm^2 after polarization at 250 °C for 33 h. The corresponding R_P also dramatically increased from 0.31 to 1.32 Ω cm^2 (Figure 11c). The significant increase in both cell ohmic and polarization resistances is clearly attributed to the evaporation and leaching of PA in pristine PA/PBI membranes, leading to the substantially reduction in membrane proton conductivity and loss of active sites in the catalyst layer.[3b,44] This clearly indicates that operation at high temperature of 250 °C is detrimental to the performance and stability of pristine PA/PBI membranes.

The OCV of MP$_2$O$_7$/PA/PBI composite membrane fuel cells are similar to that of pristine PA/PBI membrane cells (Figure 11a). However, very different to pristine PA/PBI membrane cell, the cell voltage of SP-1/4, TP-1/4, and ZP-1/4 composite membranes increased to 0.637, 0.633 and 0.641 V, respectively, when the temperature raised to 250 °C. Most significantly, MP$_2$O$_7$/PA/PBI composite membrane cells show a much better stability. For example, the SP-1/4 cell exhibits a very stable performance over 50 h, while the voltage of ZP-1/4 cell decreases slightly to 0.564 V after polarization at 200 mA cm^{-2} at 250 °C for 48 h, showing a small degradation rate of 1.55 mV h^{-1}. The composite membrane cells show a significantly better performance and stability at 250 °C, see Figure 11d–f. Among them, the SP-1/4 composite membrane cells show the best performance and stability, achieving initial PPD of 475.6 mW cm^{-2} and reaching a final PPD of 455.4 mW cm^{-2} after tested at 250 °C for 54 h (Figure 11d). In the case of ZP-1/4 cells, the initial PPD is 420 mW cm^{-2} and decreased to 332 mW cm^{-2} after tested at 250 °C for 48 h. The EIS results reveal that the in situ formed SnP$_2$O$_7$ phase effectively inhibits the degradation of PA/PBI membrane at 250 °C. For instance, the R_{ohm} of SP-1/4 cells slightly increased from 0.09 to 0.11Ω cm^2 after tested for 54 h (Figure 11g). After about 50 h, the increases of cell polarization resistance of composite membrane cells are much smaller than that of the pristine PBI membrane cell operating at 250 °C, suggesting a positive contribution of MP$_2$O$_7$ for the stabilization of the electrode activity.[40] Nevertheless, the inhibiting effect of metal pyrophosphates depends strongly on the nature of the in situ formed MP$_2$O$_7$ phase. In the case of ZP-1/4 cells, the initial R_{ohm} is 0.11 Ω cm^2 and increases quickly to 0.32 Ω cm^2 after tested at 250 °C for 48 h due to the loss of proton conductivity of the membrane (Figure 11i). This appears to be related to the coarse microstructure and difficult in the formation of
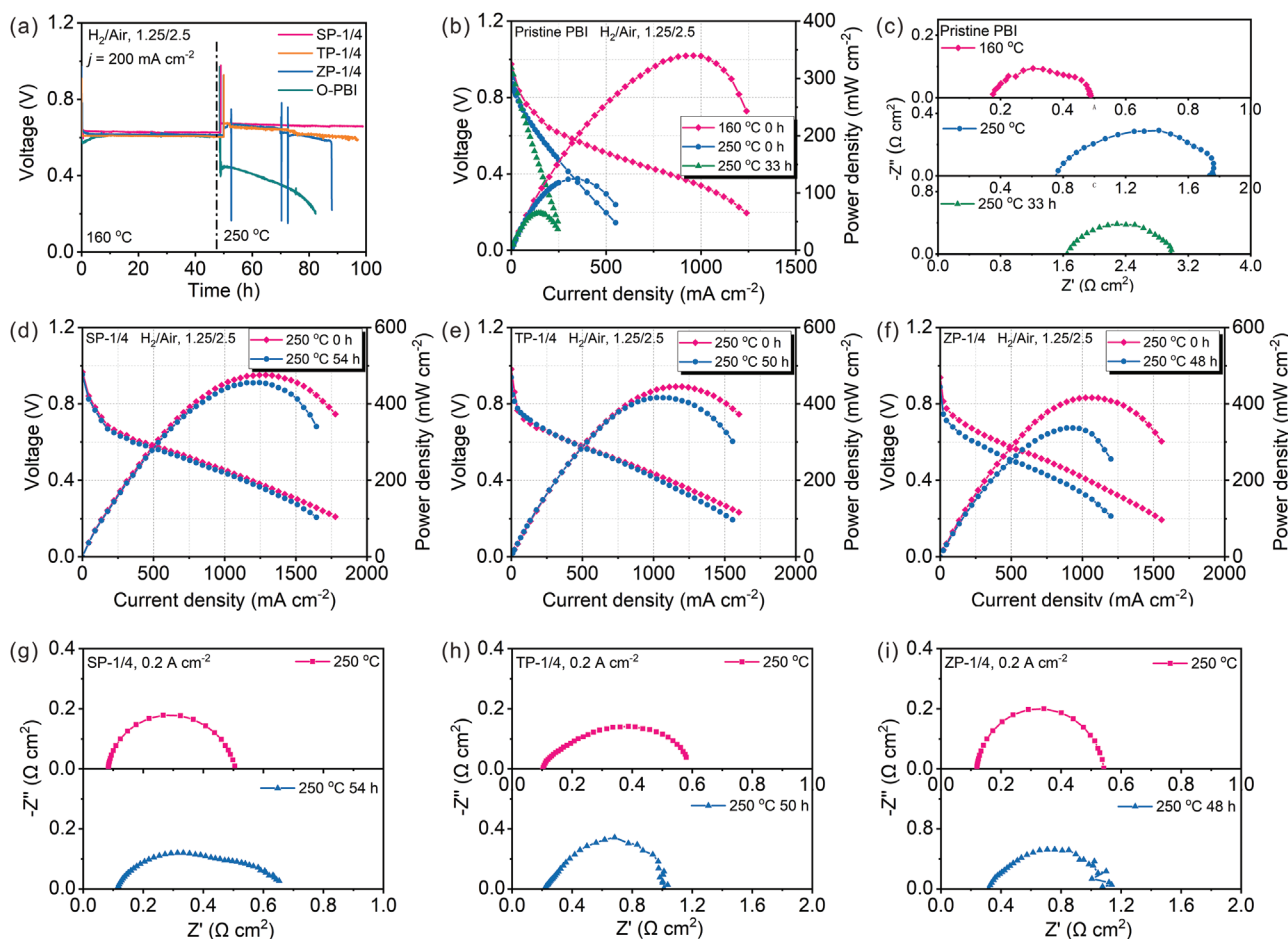
Figure 11. a) Preliminary stability test of pristine PBI, SP-1/4, TP-1/4, and ZP-1/4 fuel cells at 160 and 250 °C with the constant current density of 200 mA cm^{-2}. b) Polarization curves and c) Nyquist plots of pristine PBI membrane fuel cell between 160 and 250 °C, respectively; polarization curves of d) SP-1/4, e) TP-1/4, and f) ZP-1/4 composite membrane fuel cells tested before and after stability test at 250 °C for 50 h; and corresponding Nyquist plots of g) SP-1/4, h) TP-1/4, and i) ZP-1/4 composite membrane fuel cells before and after stability test at 250 °C.

amorphous layer on the surface of ZrP_2O_7 particles formed in the PBI matrix (see Figures 2 and 3).

The presence of in situ formed MP_2O_7 also inhibits the agglomeration of Pt/C electrocatalysts. The initial average particle size of Pt nanoparticles in Pt/C catalyst was 2.52 nm and increased significantly to 5.12 nm after testing in PA/PBI membrane cell at 250 °C for 50 h (Figure S10a–d, Supporting Information). This is consisting with the results that high temperature promotes the agglomeration of Pt nanoparticles.[26a,47] Interestingly, in the case of MP_2O_7/PA/PBI composite membrane cells, the agglomeration of Pt nanoparticles was relatively slow, increasing to 4.44 nm for SP-1/4 cells, 4.64 nm for TP-1/4 cells, and 5.07 nm for ZP-1/4 cells, respectively, smaller than 5.12 nm observed on pristine PA/PBI membrane cells tested under identical conditions. The growth of Pt particles in acidic medium is considered through Ostwald ripening, in which high temperature and acidity accelerate the initial process of Pt dissolution.[48] The reduced agglomeration of the Pt catalyst in electrode is most likely due to the reduced leaching of PA from MP_2O_7/PA/PBI composite membrane.[26a,40,49]

The single cell performance of the composite membranes was carried out on selected SP-1/4, TP-1/4, and ZP-1/4 com-

posite membrane at different temperatures and the results are shown in **Figure 12**. Prior to the performance measurement, the cells were treated at a constant voltage of 0.6 V and 250 °C for 48 h to in situ form MP_2O_7 phase in the composite membranes. The results indicate the strong dependence of the cell performance on the operation temperature. For instance, the PPD of SP-1/4 membrane cell is 394.6 mW cm^{-2} at 160 °C and increases with the operation temperature, reaching a maximum value of 482.2 mW cm^{-2} at 240 °C. Further increase of the temperature to 260 °C leads to slightly decreased PPD to 466.8 mW cm^{-2} (Figure 12a). Similar polarization behavior was also observed on TP-1/4 and ZP-1/4 membrane cells, reaching maximum PPD of 415 and 436 mW cm^{-2} at 240 °C, respectively (see Figure 12c,e). In the case of SP-1/4 membrane cell, R_{ohm} of the cell is stable, ≈0.09 Ω cm^2 in the temperature range of 160–260 °C in this study. In the case of TP-1/4 cell, R_{ohm} changed slightly from 0.13 to 0.15 Ω cm^2 in the temperature range of 160–260 °C, while in the case of ZP-1/4 cells, the R_{ohm} decreased from initial 0.16 Ω cm^2 at 160 °C to 0.13 Ω cm^2 at 260 °C (see Figure 12f).

To better evaluate the durability of composite membranes, an accelerated stress test (AST) method proposed by Schonvogel
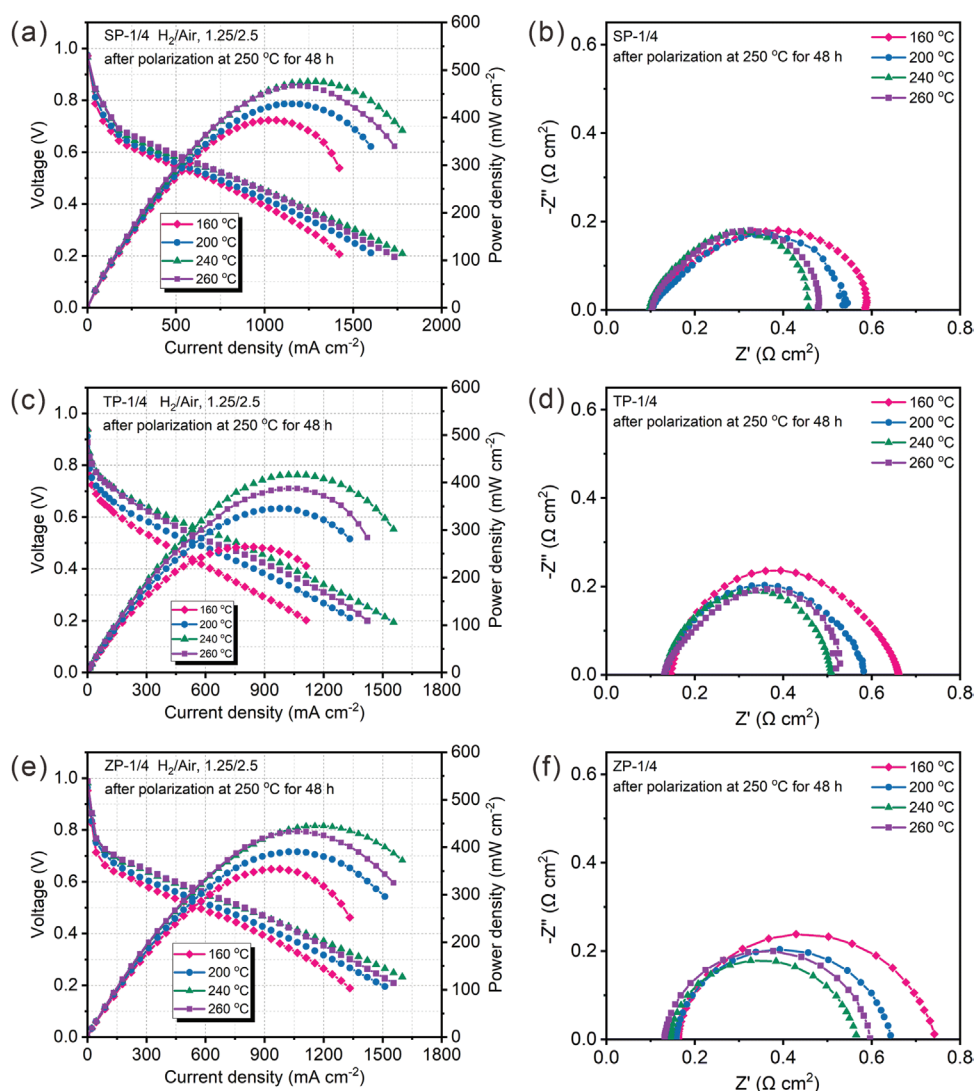
Figure 12. Polarization curves of a) SP-1/4, c) TP-1/4, and e) ZP-1/4 composite membrane cells operated between 160 and 260 °C after polarization at 250 °C for 48 h with a constant voltage of 0.6 V and the corresponding EIS Nyquist plots of b) SP-1/4, d) TP-1/4, and f) ZP-1/4 composite membrane cells at a voltage of 0.6 V under H_2/air condition.

et al.[50] was adopted to test the pre-polarized SP-1/4 and ZP-1/4 membrane cells. Li et al. revealed that high current density accelerates the overall degradation of PBI membrane, including the increased water production and PA migration.[3b] As shown in **Figure 13**a, all membrane cells exhibit performance degradation in AST test. In the case of SP-1/4 composite membrane cell, the degradation rate measured at OCV, 0.6 A cm^{-2} and 1.0 A cm^{-2} is 1.07 mV h^{-1}, 1.29 mV h^{-1}, and 2.91 mV h^{-1}, respectively, after tested at 250 °C for 55 h. On the other hand, ZP-1/4 composite membrane cell shows a much higher performance degradation and the degradation rate measured at OCV, 0.6 A cm^{-2} and 1.0 A cm^{-2} is 15.9 mV h^{-1}, 16.6 mV h^{-1}, and 17.5 mV h^{-1}, respectively. This indicates that the PA retention ability in the composite membrane strongly depend on the nature of the in situ formed metal pyrophosphates. The ZP-1/4 membrane cell shows a significant reduction in the power output and is 227.3 mW cm^{-2} after AST test at 250 °C for 17 h, significantly

lower than 274.9 mW cm^{-2} of the SP-1/4 membrane cell after AST test for 57 h (see Figure 13b,c).

The performance degradation process in selected SP-1/4 and ZP-1/4 composite membranes was further investigated by measurement of the hydrogen crossover of the cells before and after the AST. As shown in Figure 13d, the initial crossover current density of SP-1/4 and ZP-1/4 membrane cells is similar. However, a dramatic increase of crossover current density was detected in the ZP-1/4 membrane cell after 17 h test, illustrating a high permeation of hydrogen from the anodic side to the cathodic side. This is most likely due to the agglomeration of ZrP_2O_7 during the AST and the deterioration of the overall structure of membrane, which increases the porosity and creates cracks that allow hydrogen to penetrate the membrane. Therefore, this would result in the drastic decrease of OCV and performance of the cell.[42,51] This is supported by the significant reduction in PPD form initial
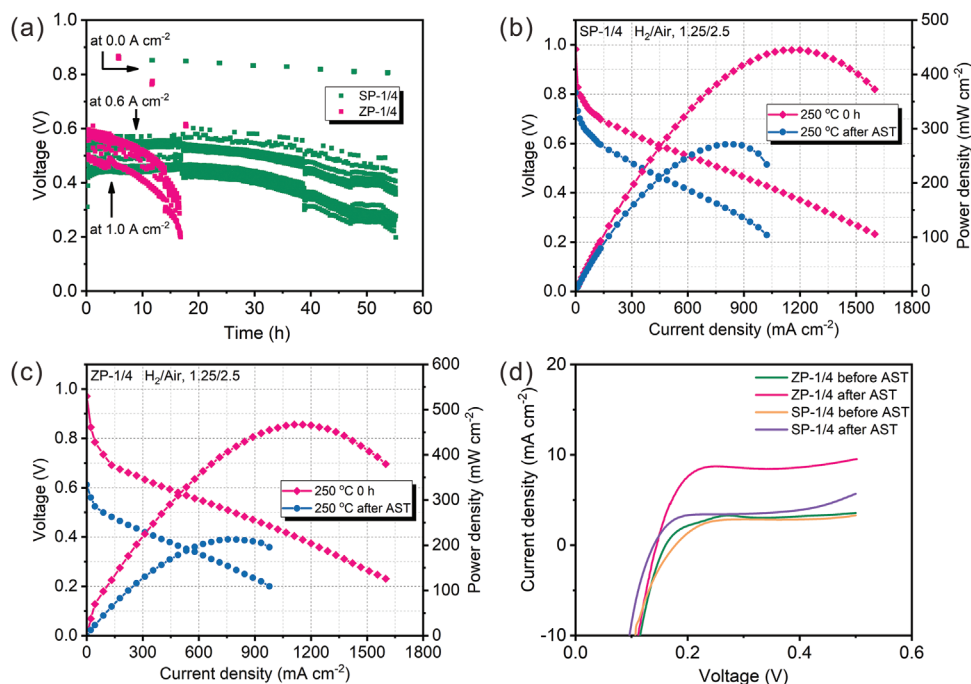
Figure 13. a) Durability test and of SP-1/4 and ZP-1/4 composite membrane cells under AST condition; Polarization curves of b) SP-1/4 and c) ZP-1/4 composite membrane cells before and after AST test at 250 °C. d) Hydrogen crossover current densities of SP-1/4 and ZP-1/4 cells before and after AST test.

462–217 mWcm^{-2} after AST for 17 h (Figure 13c). By contrast, SP-1/4 composite membrane cell showed a much stable polarization performance, maintaining a PPD of 274 mWcm^{-2} from initial 447 mWcm^{-2} after AST for 57 h. This is consistent with the more or less similar hydrogen crossover behavior before and after the AST, indicating the much better interface between the in situ formed SnP_2O_7 phase and PBI matrix of the composite membrane.

The current study evidently shows that the in situ formed MP_2O_7 phase has the capability to hold proton-conducting pyrophosphoric acid in the PBI matrix, which results in the significant improved performance and stability of the composite membrane cells as compared to pristine PA/PBI membrane cells. The results also demonstrate that the acid-holding effect of the in situ formed metal pyrophosphates depends strongly on the properties of the in situ formed metal pyrophosphates, which is closely related to the microstructure and nature of the amorphous layer formed. As shown above, both TiP_2O_7 and ZrP_2O_7 tend to aggregate into large particles and have less capability in the formation of thin and irregular amorphous layer on the particle surface. This is particularly the case for ZrP_2O_7 with large aggregated particles and clean surface morphology with no amorphous layer (see Figure 3h), resulting in a limited effect for inhibiting acid loss and reduced stability during long-term operation of cells at elevated temperature of 250 °C (Figure 12f,i). In the case of SnP_2O_7/PA/PBI composite membrane cell, the in situ formed SnP_2O_7 shows a much fine microstructure with nano-sized particles, high specific surface area and thin and irregular amorphous layer. The high proton conductivity and excellent stability of the SnP_2O_7/PA/PBI composite membrane cell also indicates the gel-like regions in the vicinities of the core–shell structure, similar to that of in situ formed phososilicate nanoclusters.[26] The presence of gel-like

region around the in situ formed SnP_2O_7 particles would be very effective to hold the acid and limit the movement of PA within the composite membranes, maintaining sufficient number of acid for the hopping and migration of protons at elevated temperatures. In contrast, in pristine PA/PBI membranes, the relatively free acid would leach out of the membrane at elevated temperatures, leading to the reduced acid lading and thus significantly reduced proton conductivity and performance at elevated temperatures. **Figure 14** shows schematically the proton conduction in pristine and SnP_2O_7/PA/PBI composite membranes. The acid-rich, gel-like region and irregular amorphous layer plays a crucial role in the high and stable conductivity at elevated temperatures. Such core–shell structure of the in situ formed metal pyrophosphates (MP_2O_7) nanoclusters can substantially reduce the vapor pressure and alleviate the acid loss via evaporation in the composite membranes at elevated temperatures.

3. Conclusion

In this work, the synthesis and characterization of in situ formed metal pyrophosphates (MP_2O_7, where M = Sn, Ti, and Zr) in phosphoric acid doped PA/PBI (MP_2O_7/PA/PBI) composite membranes for HT-PEMFCs were reported in detail. The characteristics and properties of MP_2O_7 synthesized from metal oxides/phosphoric acid (PA) depends strongly on the nature of metal pyrophosphates. In comparison with TiP_2O_7 and ZrP_2O_7 prepared under identical conditions, SnP_2O_7 has the smallest particle size, highest specific surface area, best acid retention capability, and proton conductivity. The results show that in situ formed MP_2O_7/PA/PBI composite membrane can effectively inhibit the leaching and evaporation of PA at elevated
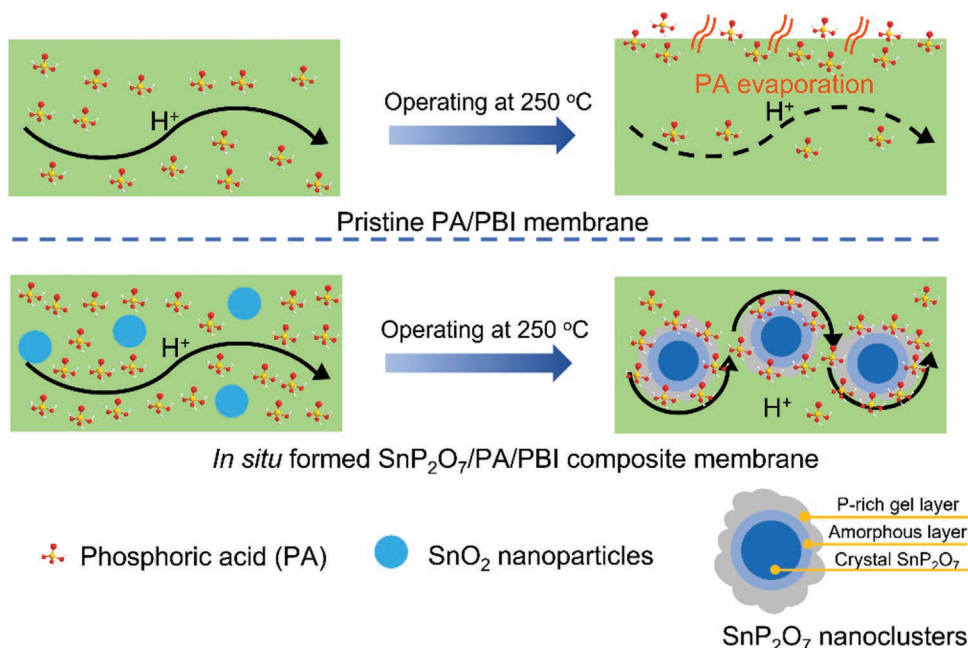
Figure 14. Schematic illustration of the proton transfer mechanism of the pristine PA/PBI membrane and the in situ formed SnP_2O_7/PA/PBI composite membrane at high operating temperature of 250 °C.

temperature and demonstrate high performance and significantly better stability at high temperature of 250 °C as compared to quick deterioration of cell performance of pristine PA/PBI membrane cells tested under identical conditions.

However, the promotion effect of in situ formed MP_2O_7 is closely related to the microstructure and characteristics of metal pyrophosphates. Among MP_2O_7/PA/PBI composite membranes, in situ formed SnP_2O_7 phase is uniformly distributed within PBI matrix due to the slow reaction rate of SnO_2 and PA, while TiP_2O_7 and ZrP_2O_7 tend to aggregate, leading to phase separation. The growth of TiP_2O_7 and ZrP_2O_7 particles is also accompanied by the formation of pores or cracks in the composite membrane, leading to the leaching of PA from membrane and the deterioration of performance at high temperatures. In contrast to TiP_2O_7 and ZrP_2O_7, the as-synthesized SnP_2O_7 is characterized by the presence of a distinct, irregular and thin amorphous layer on the surface of SnP_2O_7 particles, forming typical core–shell structure. The results show that such in situ formed irregular and thin amorphous layer has the ability to hold gel-like region in its vicinities, effectively to retain acid within the composite membranes and inhibit the acid leaching, leading to the excellent high proton conductivity and high durability at elevated temperatures. The in situ formed SnP_2O_7/PA/PBI composite membrane cell achieved a high PPD of 475.6 mW cm^{-2} and good stability in 57 h AST test at 250 °C. This study provides a new platform for the development of PEMFCs with operation temperatures over 200 °C.

4. Experimental Section

Preparation of Metal Pyrophosphates: ZrO_2, TiO_2, and SnO_2 nanoparticles with the average size of 50 nm were purchased from Macklin reagent, China. Phosphoric acid (85% H_3PO_4, PA), dimethylacetamide (DMAC), and ethanol were bought from Peking reagent CO., LTD., China. Pt/C (40 wt% on Vulcan XC-72 carbon) was purchased from Premetek CO., USA. Poly(aryletherbenzimidazole) (O-PBI) powder was obtained from Shanghai shengJun CO., China.

SnP_2O_7, TiP_2O_7, and ZrP_2O_7 were synthesized at different temperatures to evaluate the formation mechanism of MP_2O_7. Metal oxides were mixed with PA in a PTFE beaker with continuous stirring to form a homogeneous mixture, followed by calcination at 200–250 °C for 2–48 h, denoted as SnO_2-PA, TiO_2-PA, and ZrO_2-PA, respectively. Stoichiometric ratio of metal oxides (SnO_2, TiO_2, and ZrO_2) and phosphate (P) elements was kept constant of ¼. To avoid the interference of presence of PA, the as-prepared powder was washed by deionized water and ethanol for several times to completely remove excessive PA on the surface of the sample. The conductivity of as-prepared and washed sample powders was measured after pressing to disks with the diameter of 10 mm and thickness of 2 mm using two-probe conductivity measurement technique.

Preparation of Composite Membrane and Membrane-Electrode-Assembly: Pristine PBI membrane was obtained by solution casting. In this method, 5 wt% O-PBI powder was first dissolved in 10 mL DMAC with vigorous stirring, forming a viscous dark brown solution. Then, PBI solution was filtered to remove any impurities, followed by placing the solution in an ultrasonic cleaner for several hours before casting on glass plate. The resultant membrane was obtained by heating in a vacuum oven from 60 to 120 °C for 12 h to evaporate solvent.

The preparation of composite membranes is similar to that of pristine PBI membrane. Typically, metal oxides with different content were mixed with 10 mL DMAC under stirring at 80 °C for 4 h. This was followed by adding 0.5 g O-PBI powder into the solution with further stirring for 12 h. The molar ratios of metal oxides to O-PBI were 1/5, 1/4, 1/2, 1/1, and 2/1, respectively, and the thickness of obtained membrane after drying at 120 °C for 12 h was ≈40 μm. Typically, for the composite membranes prepared with different metal oxides/O-PBI ratios were denoted as the SP-n for the SnO_2-PBI, TP-n for the TiO_2-PBI and ZP-n for the ZrO_2-PBI membranes (n is the value of ratio). Thus, for composite membranes prepared with SnO_2/O-PBI ratio of 1/4, the membrane was denoted SP-1/4. For PA doping, the membranes were immersed in 85% H_3PO_4 solution at 80 °C for 3 days.
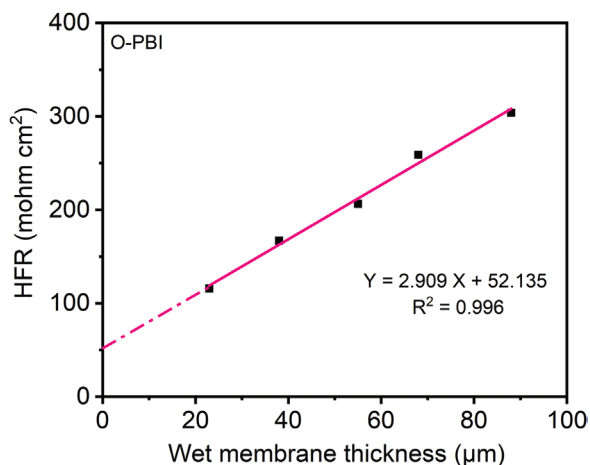
Figure 15. The total resistance obtained at high frequency intercept (R_{total}) as a function of wet membrane thickness of a pristine O-PBI membrane, measured at room temperature.

Gas diffusion layers (GDL) were purchased from Freudenberg Group, Germany. The Pt/C catalyst was dispersed on the surface of the GDL by ultrasonic spraying with the active area of 25 cm^{-2}, and the loading of catalyst was 1.2 mg cm^{-2} for cathode and 0.8 mg cm^{-2} for anode, respectively. Membrane-electrode-assembly (MEA) was fabricated by sandwiching a PA/PBI or composite membrane between two pieces of Pt/C coated GDLs, followed by hot pressing at 110 °C for 5 min with the pressure of 25 kg cm^{-2}. To form MP_2O_7 in the PA/PBI membranes in situ, the as-prepared MEA was heated at 250 °C for 48 h under a constant cell voltage 0.6 V, which is to prevent the loss of PA under open circuit at elevated temperatures.

Characterization: Powder XRD analysis of the MP_2O_7 formation was performed by using D8 Advance diffractometer, Bruker, at 40 kV and 40 mA. The data was collected between 5° and 80° in 2θ with a step of 0.15° s^{-1}. The SEM analyses of nanoparticles were carried out in Sigma 300, Zeiss. The HR-TEM analyses were performed using FEI Talos Fs200X, at 200 kV. The N_2 adsorption and desorption experiment (Micromeritics TriStar II3020, USA) was performed to investigate the specific surface area of MPPs according to the BET method. Specimens were initially heat-treated under He flow at 200 °C for 1 h and then measured at −196 °C in the liquid N_2. Temperature programmed desorption of ammonia (NH_3-TPD) and the recorded spectra from a thermal conductivity detector was measured and processed by using a chemisorption apparatus (AutoChem II 2920, USA). About 0.15 g sample was evacuated at 300 °C for 1 h before the adsorption of ammonia at room temperature. After that, the temperature was kept at 80 °C for 30 min to remove the absorbed NH_3. The reactor temperature was increased to 700 °C at the heating rate of 5 °C min^{-1} with a constant N_2 flow of 30 mL STP min^{-1}.

Electrochemical performance of as-prepared MEA assembled in homemade fuel cell rig was measured by a battery testing system (CT-4008, Neware). The stoichiometric ratio of H_2 and air was kept constant as 2.5/5 controlled by the mass flowmeter during the operation. The durability test of AST was performed alternately at 0.6 A cm^{-2} for 4 min, 1 A cm^{-2} for 16 min and at OCV for 10 min every 6 h. The EIS data of membrane was recorded at OCV and 0.6 V in the frequency range between 100 kHz and 0.1 Hz using an electrochemical workstation (Parstat 2273, Princeton Applied Research, USA). The EIS of pressed MP_2O_7 disks was measured at a frequency range of 100 kHz and 10 Hz. The hydrogen crossover current of membranes was compared by feeding hydrogen and nitrogen to anode and cathode at the flow rate of 150 mL min^{-1}, and determined from 0.01 to 0.7 V at the rate of 5 mV s^{-1}, using a CHI workstation (CHI 660E).

The through-plane proton conductivity of composite membranes was measured from EIS in the frequency range between 100 kHz and 0.1 Hz.

The membrane was sandwiched between two GDLs and assembled to a fuel cell rig. To determine the influence of electronic resistance of voltage probes, that is, the system resistance (R_{system}), the resistance measured from the high frequency intercept of the total ohmic resistance (R_{total}) of the membranes with different thicknesses was tested on the same fuel cell hardware, using pristine PBI membrane. Therefore, the ASR associates with the membrane is calculated from the equation:

$$ASR = R_{total} - R_{system} \qquad (2)$$

Figure 15 shows the total conductivity of a pristine O-PBI membrane as a function of membrane thickness. The R_{total} shows a linear dependence on the membrane thickness with an intercept at zero membrane thickness of 52.1 mΩ cm^2. This indicates that the system resistance related to the voltage probes used is 52.1 mΩ cm^2 at room temperature. Therefore, the through-plane conductivity can be obtained on following equation:

$$\sigma = \frac{t}{ASR} \qquad (3)$$

where the ASR is the ohmic resistance related to the membrane and t is the thickness of membrane.

Supporting Information

Supporting Information is available from the Wiley Online Library or from the author.

Acknowledgements

Conflict of Interest

The authors declare no conflict of interest.

Data Availability Statement

The data that support the findings of this study are available from the corresponding author upon reasonable request.

Keywords

[1] X. Lü, Y. Qu, Y. Wang, C. Qin, G. Liu, *Energy Convers. Manage.* **2018**, *171*, 1273.

[2] a) J.-M. L.e Canut, R. M. Abouatallah, D. A. Harrington, *J. Electrochem. Soc.* **2006**, *153*, A857; b) J. Zhang, D. Aili, S. Lu, Q. Li, S. P. Jiang, *Research* **2020**, *2020*, 15.

[3] a) D. Aili, D. Henkensmeier, S. Martin, B. Singh, Y. Hu, J. O. Jensen, L. N. Cleemann, Q. Li, *Electrochem. Energy Rev.* **2020**, *3*, 793; b) T. Søndergaard, L. N. Cleemann, H. Becker, T. Steenberg, H. A. Hjuler, L. Seerup, Q. Li, J. O. Jensen, *J. Electrochem. Soc.* **2018**, *165*, F3053; c) Y. Oono, A. Sounai, M. Hori, *J. Power Sources* **2013**, *241*, 87.

[4] Q. Li, R. He, R. W. Berg, H. A. Hjuler, N. J. Bjerrum, *Solid State Ionics* **2004**, *168*, 177.

[5] T.-H. Kim, S.-K. Kim, T.-W. Lim, J.-C. Lee, *J. Membr. Sci.* **2008**, *323*, 362.

[6] S. Yu, H. Zhang, L. Xiao, E. W. Choe, B. C. Benicewicz, *Fuel Cells* **2009**, *9*, 318.

[7] D. Aili, L. N. Cleemann, Q. Li, J. O. Jensen, E. Christensen, N. J. Bjerrum, *J. Mater. Chem.* **2012**, *22*, 5444.

[8] S. H. Eberhardt, M. Toulec, F. Marone, M. Stampanoni, F. N. Buchi, T. J. Schmidt, *J. Electrochem. Soc.* **2015**, *162*, F310.

[9] H. Becker, U. Reimer, D. Aili, L. N. Cleemann, J. O. Jensen, W. Lehnert, Q. Li, *J. Electrochem. Soc.* **2018**, *165*, F863.

[10] a) M. S. Herdem, M. Y. Sinaki, S. Farhad, F. Hamdullahpur, *Int. J. Energy Res.* **2019**, *43*, 5076; b) J. Zhang, Y. Xiang, S. F. Lu, S. P. Jiang, *Adv. Sustainable Syst.* **2018**, *2*, 1700184.

[11] V. S. Sikarwar, M. Zhao, P. S. Fennell, N. Shah, E. J. Anthony, *Prog. Energy Combust. Sci.* **2017**, *61*, 189.

[12] D. Wichmann, P. Engelhardt, R. Wruck, K. Lucka, H. Köhne, *ECS Trans.* **2010**, *26*, 505.

[13] a) Y. Cheng, J. Zhang, S. F. Lu, S. P. Jiang, *J. Power Sources* **2020**, *450*, 227620; b) W. R. Yan, Y. Xiang, J. Zhang, S. F. Lu, S. P. Jiang, *Adv. Sustainable Syst.* **2020**, *4*, 2000065.

[14] S. Yu, L. Xiao, B. C. Benicewicz, *Fuel Cells* **2008**, *8*, 165.

[15] P. Mocoteguy, B. Ludwig, J. Scholta, Y. Nedellec, D. J. Jones, J. Roziere, *Fuel Cells* **2010**, *10*, 299.

[16] a) Z. Guo, M. Perez-Page, J. Chen, Z. Ji, S. M. Holmes, *J Energy Chem.* **2021**, *63*, 393; b) J. Zhang, S. Chen, H. J. Bai, S. F. Lu, Y. Xiang, S. P. Jiang, *Int. J. Hydrogen Energy* **2021**, *46*, 11104.

[17] Y. Özdemir, N. Üregen, Y. Devrim, *Int. J. Hydrogen Energy* **2017**, *42*, 2648.

[18] F. J. Pinar, P. Cañizares, M. A. Rodrigo, D. Úbeda, J. Lobato, *J. Power Sources* **2015**, *274*, 177.

[19] a) Y. X. Ooi, K. Z. Ya, K. Maegawa, W. K. Tan, G. Kawamura, H. Muto, A. Matsuda, *Solid State Ionics* **2020**, *344*, 115140; b) R. He, Q. Li, G. Xiao, N. J. Bjerrum, *J. Membr. Sci.* **2003**, *226*, 169.

[20] a) T. Anfimova, T. Lie-Andersen, E. P. Jensen, C. B. Prag, U. G. Nielsen, D. R. Sørensen, E. M. Skou, E. Christensen, N. J. Bjerrum, Q. Li, *Solid State Ionics* **2015**, *278*, 209; b) C. R. Kreller, H. H. Pham, M. S. Wilson, R. Mukundan, N. Henson, M. Sykora, M. Hartl, L. Daemen, F. H. Garzon, *J. Phys. Chem. C* **2017**, *121*, 23896.

[21] Y. Jin, Y. Shen, T. Hibino, *J. Mater. Chem.* **2010**, *20*, 6214.

[22] G. Y. Foran, G. R. Goward, *J. Phys. Chem. C* **2020**, *124*, 28407.

[23] a) C. R. Kreller, M. S. Wilson, R. Mukundan, E. L. Brosha, F. H. Garzon, *ECS Electrochem. Lett.* **2013**, *2*, F61; b) X. Wu, A. Verma, K. Scott, *Fuel Cells* **2008**, *8*, 453; c) S. Tao, *Solid State Ionics* **2009**, *180*, 148.

[24] a) R. A. Krueger, L. Vilčiauskas, J.-P. Melchior, G. Bester, K.-D. Kreuer, *J. Phys. Chem. B* **2015**, *119*, 15866; b) K. Miyazaki, Y. Kato, T. Matsui, S. Hayashi, Y. Iriyama, T. Fukutsuka, T. Abe, Z. Ogumi, *Phys. Chem. Chem. Phys.* **2012**, *14*, 11135.

[25] Y. C. Jin, M. Nishida, W. Kanematsu, T. Hibino, *J. Power Sources* **2011**, *196*, 6042.

[26] a) J. Zhang, D. Aili, J. Bradley, H. H. Kuang, C. Pan, R. De Marco, Q. F. Li, S. P. Jiang, *J. Electrochem. Soc.* **2017**, *164*, F1615; b) D. Aili, J. Zhang, M. T. D. Jakobsen, H. J. Zhu, T. Y. Yang, J. Liu, M. Forsyth, C. Pan, J. O. Jensen, L. N. Cleemann, S. P. Jiang, Q. F. Li, *J. Mater. Chem. A* **2016**, *4*, 4019.

[27] a) H. B. Ortíz-Oliveros, R. M. Flores-Espinosa, E. Ordoñez-Regil, S. M. Fernández-Valverde, *Chem. Eng. J.* **2014**, *236*, 398; b) G. R. Genoveva, O. R. Enrique, R. G. E. Teresita, O. R. Eduardo, *J. Miner. Mater. Charact. Eng.* **2007**, *6*, 39.

[28] L. Szirtes, J. Megyeri, E. Kuzmann, *J. Therm. Anal. Calorim.* **2010**, *99*, 415.

[29] M. Ma, S. Guo, W. Shen, *ACS Appl. Mater. Interfaces* **2018**, *10*, 2612.

[30] M. S. Kishore, V. Pralong, V. Caignaert, U. V. Varadaraju, B. Raveau, *J. Power Sources* **2007**, *169*, 355.

[31] U. Costantino, R. Vivani, V. Zima, E. Cernoskova, *J. Solid State Chem.* **1997**, *132*, 17.

[32] X. Xu, S. Tao, P. Wormald, J. T. S. Irvine, *J. Mater. Chem.* **2010**, *20*, 7827.

[33] Y. Li, T. Kunitake, E. Aoki, E. Muto, *Adv. Mater.* **2008**, *20*, 2398.

[34] T. Hibino, K. Kabayashi, S. Fujita, *J. Mater. Chem. A* **2013**, *1*, 13082.

[35] M. Yamada, D. Li, I. Honma, H. Zhou, *J. Am. Chem. Soc.* **2005**, *127*, 13092.

[36] F. Lónyi, J. J. M. Valyon, *Microporous Mesoporous Mater.* **2001**, *47*, 293.

[37] N. Katada, M. Niwa, *Catalysis Surveys from Asia* **2004**, *8*, 161.

[38] D. W. Smith, *J. Chem. Educ.* **1987**, *64*, 480.

[39] A. S. Wagh, S. Y. Jeong, *J. Am. Ceram. Soc.* **2003**, *86*, 1838.

[40] J. Zhang, D. Aili, J. Bradley, H. Kuang, C. Pan, R. De Marco, Q. Li, S. P. Jiang, *J. Electrochem. Soc.* **2017**, *164*, F1615.

[41] G. Nawn, G. Pace, S. Lavina, K. Vezzù, E. Negro, F. Bertasi, S. Polizzi, V. Di Noto, *ChemSusChem* **2015**, *8*, 1381.

[42] Z. Guo, J. Chen, J. J. Byun, M. Perez-Page, Z. Ji, Z. Zhao, S. M. Holmes, *J. Membr. Sci.* **2022**, *641*, 119868.

[43] H. Bai, H. Peng, Y. Xiang, J. Zhang, H. Wang, S. Lu, L. Zhuang, *J. Power Sources* **2019**, *443*, 227219.

[44] J. Zhang, H. Bai, W. Yan, J. Zhang, H. Wang, Y. Xiang, S. Lu, *J. Electrochem. Soc.* **2020**, *167*, 114501.

[45] Y. Liu, J. Wang, H. Zhang, C. Ma, J. Liu, S. Cao, X. Zhang, *J. Power Sources* **2014**, *269*, 898.

[46] J.-P. Melchior, K.-D. Kreuer, J. Maier, *Phys. Chem. Chem. Phys.* **2017**, *19*, 587.

[47] Y. Oono, T. Fukuda, A. Sounai, M. Hori, *J. Power Sources* **2010**, *195*, 1007.

[48] S. Mitsushima, Y. Koizumi, S. Uzuka, K.-I. Ota, *Electrochim. Acta* **2008**, *54*, 455.

[49] S. Matar, A. Higier, H. Liu, *J. Power Sources* **2010**, *195*, 181.

[50] D. Schonvogel, M. Rastedt, P. Wagner, M. Wark, A. Dyck, *Fuel Cells* **2016**, *16*, 480.

[51] K. P. Ramaiyan, S. Herrera, M. J. Workman, T. A. Semelsberger, V. Atanasov, J. Kerres, S. Maurya, Y. S. Kim, C. R. Kreller, R. Mukundan, *J. Mater. Chem. A* **2020**, *8*, 16345.